Safety-Aware Hybrid Control of Airborne Wind Energy Systems

Nikolaus Vertovec *
Department of Engineering Science, University of Oxford Parks Road, OX1 3PJ, UK

Sina Ober-Blöbaum †
Department of Mathematics, Paderborn University, 33100, Germany

Kostas Margellos ‡
Department of Engineering Science, University of Oxford Parks Road, OX1 3PJ, UK

A fundamental concern in progressing Airborne Wind Energy (AWE) operations toward commercial success, is guaranteeing that safety requirements placed on the systems are met. Due to the high dimensional complexity of AWE systems, however, formal mathematical robustness guarantees become difficult to compute. We draw on research from Hamilton-Jacobi (HJ) reachability analysis to compute an avoidance control maneuver for the path-following controller that enforces safety constraints on the system while maintaining the guidance strategy. In addition, the zero-sublevel set of the computed value function inherent in HJ reachability analysis indicates the backward reachable set, the set of states from which it is possible to safely drive the system into a target set within a given time without entering undesirable states. Furthermore, to integrate the avoidance controller with the path-following controller, we derive the necessary switching law such that the avoidance maneuver is only initiated when a tether rupture is potentially imminent. We illustrate our results via extensive simulation-based studies.

I. Introduction

With the looming threat of the climate crisis becoming ever more detrimental, the need for low-cost and reliable sources of energy becomes increasingly pressing. Wind remains the primary non-hydro renewable and to reach net-zero energy targets of 8008 TWh in 2030, will need to grow annually by 18% between 2021 and 2030 [1]. Conventional wind turbines have high material costs and often struggle with unreliable wind patterns present at low altitudes. Airborne Wind Energy (AWE) systems solve many of the problems of conventional wind turbines by harnessing wind energy at high altitudes, where stronger and more reliable wind currents can be found. Thus, over the past decade, we have seen a rapid increase in research and development into AWE from both academia and the private sector [2, 3].

In this paper, we only consider Ground-Gen systems, whereby energy is obtained by continuously performing two phases of flight, a *traction* phase, and a *retraction* phase. During the traction phase, a tethered kite or fixed-wing aircraft

*Doctoral Student, Department of Engineering Science, University of Oxford; nikolaus.vertovec@eng.ox.ac.uk (Corresponding Author)
†Professor, Department of Mathematics, Paderborn University; sinaober@math.uni-paderborn.de
‡Associate Professor, Department of Engineering Science, University of Oxford; kostas.margellos@eng.ox.ac.uk

is flown in crosswind conditions at altitudes of up to 1000m above ground. The traction force acting on the aircraft's tether is converted into electricity using a generator and winch located at the base of the tether [4, 5]. For a discussion of alternative AWE systems, we refer to [5, 6]. Since the tether is gradually reeled out during the traction phase, the system will eventually need to be reset. For this, the aircraft is flown back to its starting altitude upwind in a phase commonly referred to as the retraction phase. During the retraction phase, a small amount of the previously generated energy needs to be spent on reeling in the tether. Nevertheless, AWE systems have been shown to be able to create a high net energy output, with SkySails' recent uninterrupted automated flight of 42 hours producing 62 kW of average power and average power over the pumping cycle of approximately 92 kW [7], while larger systems aim at producing energy in the range of MWs [8].

For AWE systems to become widely adopted, it is necessary to provide formal guarantees on their safe operation and control. While recent research has been concentrated on improving reliability and safety of AWE [9], much of the literature, particularly on the control of AWE, focuses on performance optimization [10–14]. The aim of this paper in contrast, is to ensure safety of an AWE system while maintaining optimal power generation abilities. To this end, we propose a hybrid control law, whereby a safety controller is only activated when a critical system failure is predicted to occur. Incorporating safety by these means, effectively defining an avoidance maneuver, has become a common practice in the safety-critical control literature [15], and has been effectively demonstrated in the context of AWE in [16]. In [16] the authors use nonlinear dynamic inversion (NDI), utilizing a tether force set point during the dynamic inversion in conjunction with a winch control tether force tracking strategy. Using a predictor, such as a support vector machine, trained to detect upset conditions, an avoidance strategy is derived by means of reducing the tether force set point.

In contrast to the empirical avoidance strategy proposed in [16], we present a safety controller derived using reachability analysis, thus guaranteeing satisfaction of hard constraints encoding safety. The proposed avoidance maneuver is derived independently of the chosen winch strategy and incorporates uncertainty in, e.g. wind conditions, through the incorporation of adversarial disturbances in the control design.

We consider an AWE setup similar to that proposed in [17], whereby a fixed-wing aircraft is flown in a figure of eight flight pattern, controlled using NDI. While further extensions to the simple NDI setup can be included to assist safety, such as dealing with model uncertainty by means of incremental nonlinear dynamic inversion [18], or the avoidance strategies proposed in [16], for the sake of demonstrating the effects of our proposed avoidance maneuvers, such extensions are omitted. To set the control problem, we consider an NDI controller that is using pseudo control inputs to choose the bank angle and angle of attack so as to track a desired course and path angle for optimal tracking of a figure eight flight path. As can be seen in Fig. 1, the tether ruptures before the aircraft can complete one full cycle of flight. Using Hamilton-Jacobi (HJ) reachability analysis, we will synthesize a safety controller as well as switching conditions, such that in a hybrid control setup, minimal penalties on power generation are incurred, while ensuring a safe flight without tether rupture.

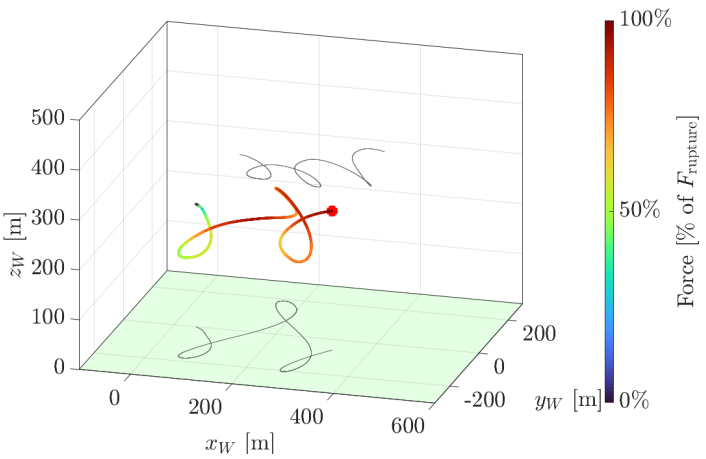

Fig. 1 Tether rupture during the traction phase. The red dot marks the point during flight at which a tether rupture occurs due to the maximum tether force being exceeded.

HJ reachability analysis has become a well-adopted formal verification method, whereby the optimal controller is derived through computation of the backward reachable set (BRS). Its advantages include compatibility with nonlinear system dynamics, formal treatment of nonlinear bounds, and recently also with multi-objective optimization problems [19, 20]. However, since HJ reachability analysis requires solving a quasi-variational inequality over a gridded state space, it is subject to the curse of dimensionality. As such, its applications have been limited to low-dimensional systems [21].

To this end, we will derive a novel low-dimensional formulation of the system dynamics of AWE systems and formulate the safety-critical control problem as a differential game of two players. Furthermore, for numerical reasons that will become evident later on, we are required to grid the state space, thus necessitating a coordinate transformation that ensures only relevant states are considered for controller synthesis, minimizing numerical overhead. Thus the key contributions of this paper are:

1) The development of a simplified low dimensional AWE model that is accurate enough for safety-critical control purposes (Section III);
2) The synthesis and deployment of an avoidance control strategy based on the developed abstractions and HJ reachability analysis, a non-trivial application for which we have made the code and simulation environment available (Section IV). This sets the framework for the development of a hybrid control law that allows switching between any performance-oriented controller and the developed safety controller;
3) The computation of the optimal control/disturbance actions that optimize the Hamiltonian of the underlying optimal control problem, which is case-dependent and non-trivial in the setting (Section IV.B);
4) The validation of the performance of the controller by applying it to a high fidelity model, thus rendering our controller as an add-on to existing tools to guarantee safety (Section V).

The remainder of the paper is organized as follows: Section II discusses the AWE model used for simulation purposes as well as the guidance strategy employed by the primary controller. Section III introduces the simplifications, abstractions, and the new reference frame used to derive a low dimensional model of the AWE system suitable for safety-control synthesis, with the safety controller being derived and introduced in Section IV. Finally, in Section V we validate the avoidance control strategy in its hybrid control setup using the high fidelity AWE model and discuss the effects on power generation with Section VI providing concluding remarks.

II. Modeling

The modeling of AWE systems has been well studied and a variety of definitions for the equations of motion have been derived. Yet commonly AWE systems require a high number of states in order to accurately capture both the dynamics of the kite or aircraft as well as the tether and the associated winch controller. Since the goal of this paper is to derive a safety-critical controller for the AWE system using HJ reachability analysis, we seek the development of a simplified yet accurate enough, from a control point of view, model.

In the following section, we begin by modeling the AWE system based predominantly on the work of [17] with extensions taken from [22, 23] and [24]. This model will be used for simulation purposes in Section V and is presented to provide the necessary notation and understanding needed for the abstractions and synthesis, the primary contributions of this work, in Sections III and IV.

A. Reference Frames

For the discussion of the dynamics of AWE systems, it is useful to introduce a variety of reference frames. The utilized reference frames (with the exception of the Γ frame, Section III.C) are common for AWE systems and have been extensively discussed in [17] and [25]. For the transformation from one reference frame to another, we introduce the transformation matrices $\mathbf{M}_{(\cdot)(\cdot)}$, where the first subscript indicates the destination frame and the second subscript indicates the origin frame. Thus, as an example, the kinematic velocity in the τ frame, where τ denotes one of the employed frames, can be obtained from the body fix frame (B) by $(\mathbf{v}_\mathrm{k})_\tau = \mathbf{M}_{\tau\mathrm{B}}(\mathbf{v}_\mathrm{k})_\mathrm{B}$. The transformation matrices for the reference frames are listed in the appendix. We utilize bold notation for vectors and matrices and regular notation for scalars. Furthermore, we utilize subscripts to denote vector elements, i.e., $(v_\mathrm{k})_{\tau,\mathrm{y}}$ denotes the y component of the kinematic velocity in the τ frame.

1. Wind Frame

The wind frame (W) is a rotation of the commonly used North-East-Down (NED or O) frame. The x-axis of the W frame is aligned with the mean wind direction (denoted by ξ). We assume that the mean wind direction is such that the z-axis of the W frame points upwards and the y-axis forms a right-hand reference frame (Fig. 2).

2. Tangential Frame

The tangential frame (τ) is centered at the position of the aircraft, such that the z-axis points towards the origin of the NED frame. To this end, the x-axis points towards the north direction, while the y-axis completes a right-hand reference frame. Since the τ frame moves together with the aircraft, its location is determined using the longitude (λ) and latitude (ϕ) as well as the distance to the origin (h_τ). The tangential frame is shown in purple in Fig. 2.

3. Aerodynamic Frame

The aircraft's kinematic velocity is denoted by $\mathbf{v}_\mathrm{k}$ and is composed of the aerodynamic velocity $\mathbf{v}_\mathrm{a}$ as well as the wind velocity $\mathbf{v}_\mathrm{w}$, i.e., $\mathbf{v}_\mathrm{k} = \mathbf{v}_\mathrm{a} + \mathbf{v}_\mathrm{w}$. This relationship holds true regardless of reference frame. For a discussion of the aerodynamic velocity, we define the aerodynamic frame (A) such that the velocity vector $\mathbf{v}_\mathrm{a}$ is aligned with the x-axis. For the derivation with respect to the NED frame (shown in blue in Fig. 2), we first rotate the NED frame by the course angle χ_a and path angle γ_a, resulting in the intermediate frame $\overline{A}$ (shown in orange in Fig. 2), before tilting the frame by the bank angle μ_a. The A frame is shown in green in Fig. 2.

4. Body-Fixed Frame

The body-fixed frame (B) is used to calculate the aerodynamic forces acting on the aircraft. It can be obtained from the aerodynamic frame (shown in green in Fig. 2) using the angle of attack α_a as well as the sideslip angle β_a (the sideslip angle is neglected in this work). The B frame is shown in red in Fig. 2.

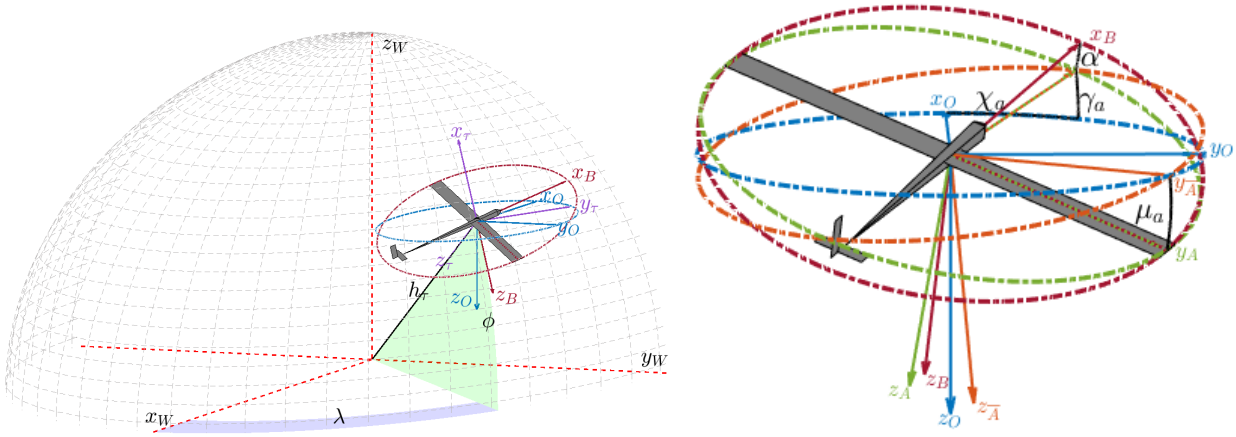

Fig. 2 Visualization of the NED frame (blue), intermediate aerodynamic frame $\overline{A}$ (orange), the aerodynamic frame A (green), the body frame B (red) and the tangential frame (purple).

B. Aircraft Equations of Motion and Ground Station Model

Since we are considering an avoidance maneuver for the path following controller, for the purpose of controller synthesis, we will assume perfect tracking of the attitude and rate controllers [17, 18]. This simplification, common

during the design of the path following controller, allows us to analyse the performance of the avoidance maneuver independent of the affects of the inner control loop. To this end, we can neglect the yaw, pitch, and roll rates as well as the sideslip angle β_a, and define out control inputs as the bank angle μ_a as well as the angle of attack α_a.

To provide a realistic conclusion on overall feasibility, we will include actuator dynamics and delays in the final simulation to represent tracking delays of the inner loop. Further validation before deployment can be performed by integrating the path following controller and avoidance maneuver into a full 6 DOF simulation, however, this is beyond the scope of this work.

The position of the aircraft is defined in the W frame by $[\lambda, \phi, h_\tau]$ and it moves with velocity v_a along the x-axis of the $\overline{A}$ frame. To connect the $\overline{A}$ frame with the NED frame, we add the course angle χ_a and path angle γ_a as additional states. To influence the heading of the aircraft, we utilize the bank angle μ_a and angle of attack α_a as inputs to the system and assume that the sideslip angle β_a is negligible, i.e., $\beta_\mathrm{a} = 0$.

Therefore our initial set of states used are $[\lambda, \phi, h_\tau, v_\mathrm{a}, \chi_\mathrm{a}, \gamma_\mathrm{a}] \in \mathbb{R}^6$. The position propagation can be calculated from the kinematic velocity in the τ frame as follows:

$$\dot{\lambda} = \frac{(v_\mathrm{k})_{\tau,\mathrm{y}}}{\cos(\phi) h_\tau}, \quad \dot{\phi} = \frac{(v_\mathrm{k})_{\tau,\mathrm{x}}}{h_\tau}, \quad \dot{h}_\tau = -(v_\mathrm{k})_{\tau,\mathrm{z}} \tag{1}$$

where $(v_\mathrm{k})_{\tau,\mathrm{x}}$, $(v_\mathrm{k})_{\tau,\mathrm{y}}$ and $(v_\mathrm{k})_{\tau,\mathrm{z}}$ denote the x, y and z components of the kinematic velocity in the τ frame, respectively. $(\mathbf{v}_\mathrm{k})_\tau$ is calculated by transforming the kinematic velocity from the O frame to the W frame, and then to the τ frame using the appropriate transformation matrix, $\mathbf{M}_\mathrm{WO}$ and $\mathbf{M}_{\tau\mathrm{W}}$, respectively, found in the appendix. $(\mathbf{v}_\mathrm{k})_\mathrm{O}$ is derived from the aerodynamic and wind velocity

$$(\mathbf{v}_\mathrm{k})_\mathrm{O} = \mathbf{M}_{\mathrm{O}\overline{\mathrm{A}}} \begin{bmatrix} v_\mathrm{a}, & 0, & 0 \end{bmatrix}^T_{\overline{\mathrm{A}}} + (\mathbf{v}_\mathrm{W})_\mathrm{O} \tag{2}$$

By assuming the wind field stays stationary, we are able to calculate the derivative of the kinematic velocity using the gravitational force ($\mathbf{F}_\mathrm{g}$), aerodynamic force ($\mathbf{F}_\mathrm{a}$), as well as the force the tether exerts on the aircraft ($\mathbf{F}_\mathrm{t}$). For a complete derivation we refer to [17].

$$\begin{bmatrix} \dot{v}_\mathrm{a} \\ \dot{\chi}_\mathrm{a} \\ \dot{\gamma}_\mathrm{a} \end{bmatrix} = \frac{1}{m_\mathrm{a}} \begin{bmatrix} 1 & 0 & 0 \\ 0 & \frac{1}{v_\mathrm{a} \cos\gamma_\mathrm{a}} & 0 \\ 0 & 0 & -\frac{1}{v_\mathrm{a}} \end{bmatrix} \left(\mathbf{M}_{\overline{\mathrm{A}}\mathrm{O}} [(\mathbf{F}_\mathrm{g})_\mathrm{O} + (\mathbf{F}_\mathrm{t})_\mathrm{O}] + \mathbf{M}_{\overline{\mathrm{A}}\mathrm{A}} \mathbf{M}_\mathrm{AB} (\mathbf{F}_\mathrm{a})_\mathrm{B} \right) \tag{3}$$

where m_a denotes the mass of the aircraft. Note that the matrix $\mathbf{M}_{\overline{\mathrm{A}}\mathrm{O}}$ depends on the course and path angles χ_a and γ_a, $\mathbf{M}_{\overline{\mathrm{A}}\mathrm{A}}$ depends on the bank angle μ_a and $\mathbf{M}_\mathrm{AB}$ depends on the angle of attack α_a and sideslip angle β_a.

1. Ground Station Model

The ground station serves as the power generator for the AWE system. The winch controller within the ground station is responsible for determining an appropriate torque so as to reel out or reel in the tether during flight. Various reeling strategies exist in the literature with the most common focussing on aligning the reel-out speed to one-third of the wind speed [26] or less when considering the retraction phase [27]. This is done in practice by either setting the torque proportional to the reel-out velocity squared [28–30] or by using reference tracking [13].

Since the winch will be modeled as an adversarial disturbance for controller synthesis, the reeling strategy can be chosen so as to determine tighter bounds on the possible range of disturbances, by, e.g., restricting the tether to only be reeled out using a positive torque. To demonstrate the efficacy of the avoidance strategy derived in sequel, however, we do not wish to limit the disturbance range by these means and instead account for a wider range of winching strategies, i.e. including the possibility of reeling in the tether during traction. To this end, a tether set point tracking strategy [31] is employed.

2. Gravitational and Aerodynamic Forces

The gravitational force can simply be expressed in the O frame as

$$(\mathbf{F}_{\mathrm{g}})_{\mathrm{O}} = \begin{bmatrix} 0, & 0, & m_{\mathrm{a}} g \end{bmatrix}^T \in \mathbb{R}^3 \tag{4}$$

where g is the gravitational constant. As mentioned earlier, we assume yaw, pitch and roll rates to be zero and neglect the effects of the sideslip angle β_{a}. This simplifies the aerodynamic coefficients derived in [22], to

$$\begin{bmatrix} C_{\mathrm{x}} \\ C_{\mathrm{y}} \\ C_{\mathrm{z}} \end{bmatrix} = \begin{bmatrix} C_{\mathrm{x},0}(\alpha_{\mathrm{a}}) + C_{\mathrm{x},\delta_{\mathrm{e}}}(\alpha_{\mathrm{a}})\delta_{\mathrm{e}} \\ C_{\mathrm{y},\delta_{\mathrm{a}}}(\alpha_{\mathrm{a}})\delta_{\mathrm{a}} + C_{\mathrm{y},\delta_{\mathrm{r}}}(\alpha_{\mathrm{a}})\delta_{\mathrm{r}} \\ C_{\mathrm{z},0}(\alpha_{\mathrm{a}}) + C_{\mathrm{z},\delta_{\mathrm{e}}}(\alpha_{\mathrm{a}})\delta_{\mathrm{e}} \end{bmatrix} \tag{5}$$

where we consider the aileron (δ_{a}), elevator (δ_{e}) and rudder (δ_{r}) deflections to be constant and all α_{a} dependent coefficients are approximated using second order polynomials. Using the aerodynamic coefficients we can then calculate the aerodynamic force of the aircraft as

$$(\mathbf{F}_{\mathrm{a}})_{\mathrm{B}} = \frac{1}{2}\rho \mathrm{S}_{\mathrm{ref}} v_{\mathrm{a}}^2 \begin{bmatrix} C_{\mathrm{x}}, & C_{\mathrm{y}}, & C_{\mathrm{z}} \end{bmatrix}^T \tag{6}$$

where $\mathrm{S}_{\mathrm{ref}}$ is the aerodynamic reference area corresponding to the projected surface area of the aircraft wing [22], and ρ is the air density.

3. Tether Forces

For the calculation of the tether forces ($\mathbf{F}_\mathrm{t}$) that act on the aircraft, we use models of varying complexity. For the controllers, we rely on a straight tether approximation, whereas for simulation purposes, we use a tether model similar to the model derived in [24]. We begin by presenting a brief overview of the lumped-mass tether model, as it provides the foundation for the simplified model used for controller synthesis, and is also used for the full simulation in Section V

Let us first consider a fixed number of lumped masses connected by n spring-damper elements. The length of each segment is denoted by l_s and the spring and damping constants for each segment are denoted by k and c, respectively. Each tether segment is modeled as a point mass with position $\mathbf{p}_i$ and velocity $\mathbf{v}_i$, as shown in Fig. 3. The equations of

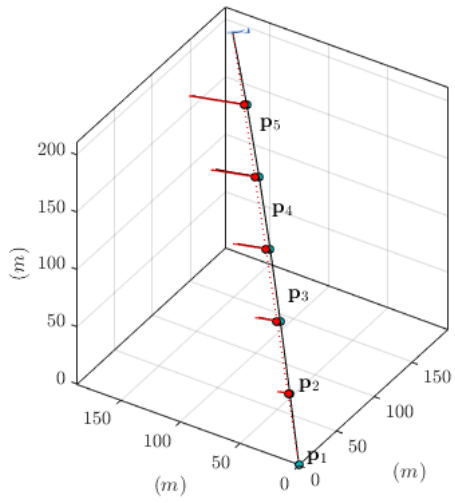

Fig. 3 Visualization of the tether modeled as a straight tether (red) and as a fixed number of lumped masses (blue). The velocities of the point masses are shown by the red and blue vectors respectively.

motion of the tether segment are given by

$$\dot{\mathbf{p}}_i = \mathbf{v}_i, \quad \dot{\mathbf{v}}_i = m_t \mathbf{F}_i \tag{7}$$

where m_t is the mass of an individual segment and $\mathbf{F}_i$ is the tether segment force. The tether segment force for segment i is given by

$$\mathbf{F}_i = \mathbf{F}_{s,i+1} - \mathbf{F}_{s,i} - \mathbf{F}_{g,s} + \mathbf{F}_{a,i} \tag{8}$$

where $\mathbf{F}_{g,s}$ is the gravitational force acting on the tether segment, $\mathbf{F}_{a,i}$ is the aerodynamic drag acting on the i-th segment, and $\mathbf{F}_{s,i}$ is the tensile force of the i-th segment.

The tensile force is calculated according to Hooke's law

$$\mathbf{F}_{s,i} = \left(k(||\mathbf{s}_i||_2 - l_s) + c\left(\frac{\mathbf{s}_i}{||\mathbf{s}_i||_2}\mathbf{s}_{v,i}\right)\right)\frac{\mathbf{s}_i}{||\mathbf{s}_i||_2} \tag{9}$$

where $\mathbf{s}_i = \mathbf{p}_i - \mathbf{p}_{i-1}$ and $\mathbf{s}_{v,i} = \mathbf{v}_i - \mathbf{v}_{i-1}$. Thus the maximum tether force is exerted on the final segment attached to the aircraft, i.e., $\mathbf{F}_t = \mathbf{F}_{s,n+1}$, with $\mathbf{s}_{n+1} = \mathbf{p}_{\text{aircraft}} - \mathbf{p}_n$ and $\mathbf{s}_{v,n+1} = \mathbf{v}_{\text{aircraft}} - \mathbf{v}_n$ and $\mathbf{p}_{\text{aircraft}}$ and $\mathbf{v}_{\text{aircraft}}$ are the position and velocity, respectively, of the aircraft in Cartesian coordinates. For the tether drag calculation, we refer to [24]. Since the tether can only exert a pulling force on the aircraft, the spring and damping constants are set to zero whenever $||\mathbf{s}_i||_2 - l_s < 0$.

This complex tether model requires $6n$ additional states, where n is the number of segments used, and is therefore only suited for simulation purposes. For the controller synthesis we use a simplified tether model that relies on a straight tether approximation and is introduced in Section III.A.

4. Wind Field Model

To capture the varying wind speeds at different altitudes we employ the wind shear model provided by the MATLAB Aerospace Toolbox [32].

$$(\mathbf{v}_{\text{shear}})_{\text{O}} = W_{20} \frac{\ln(\frac{h}{z_0})}{\ln(\frac{20}{z_0})} \tag{10}$$

where h is the altitude of the aircraft in feet, z_0 is a constant equal to 0.15 feet, and W_{20} is the measured wind speed at an altitude of 20 feet.

In addition to the wind shear, we also model atmospheric turbulence in form of a continuous Dryden wind turbulence model. The Dryden model is a stochastic gust model, whereby the linear and angular velocities of the atmospheric turbulence are modeled as spatially varying stochastic processes, each with a specific power spectral density. The longitudinal, lateral, and vertical component spectra functions are provided by Military Handbook MIL-HDBK-1797B [33]. For the implementation of the Dryden model, we utilize the continuous Dryden model block provided by the MATLAB Aerospace Toolbox [32].

Finally, the wind velocity acting on the aircraft is computed by adding the turbulence to the wind shear $(\mathbf{v}_{\text{W}})_{\text{O}} = (\mathbf{v}_{\text{turb}})_{\text{O}} + (\mathbf{v}_{\text{shear}})_{\text{O}}$.

C. Optimal Flight Path and Guidance

The fundamental idea behind Ground-Gen AWE is to transfer the force from the aerodynamic lift of the aircraft or kite to the connected tether [34]. Similar to the blades of a wind turbine, this can be done by moving the aircraft perpendicular to the mean wind direction. To this end, it has become common practice in the AWE community to adopt a figure eight flight pattern. Various methods have become well-established in the AWE control community to track such a flight pattern. In [4, 13] it is shown that two target points can suffice to generate the alternating left and right turns. In [35], the turn rate law is introduced, which is demonstrated in the skysails control structure [36]. For the desired flight path of the safety controller, the choice of guidance strategy only affects the choice of the initial target set. However, the target set needs to be defined in relation to the chosen state space. To this end, the defined reference

heading of the target point approach can be used, or, to use the turn rate law, inversion of the flight dynamics can be used to obtain the desired heading [25].

Most crucial, however, is that the flight path of the safety avoidance maneuver does not overly upset the primary controller flight path, as this would impede on power performance. We thus adopt a similar guidance strategy as employed by the chosen primary controller [31], which is based on guidance law presented in [25].

For the chosen flight path, we use a Lissajous curve, Γ, lying on a sphere. The two-dimensional curve can be described by its longitude λ_Γ and latitude ϕ_Γ. We parameterize Γ on $\mathbb{S}^2$ using the arc length s. In Cartesian coordinates the curve is then given by

$$\Gamma_P(s) = \begin{bmatrix} \cos\lambda_\Gamma(s)\cos\phi_\Gamma(s) \\ \sin\lambda_\Gamma(s)\cos\phi_\Gamma(s) \\ \sin\phi_\Gamma(s) \end{bmatrix} h_\tau \tag{11}$$

For the specific Lissajous curve, we opt for the Lemniscate of Booth [31], a commonly used figure eight curve, using the height/width ratio of $a_{\text{Booth}}/b_{\text{Booth}} = 120/200$. The longitude and latitude of the Lemniscate of Booth can be calculated as follows:

$$\lambda_\Gamma(s) = \frac{1}{h_\tau}\frac{b_{\text{Booth}}\sin s}{1+(\frac{a_{\text{Booth}}}{b_{\text{Booth}}})^2\cos^2 s} \tag{12}$$

$$\phi_\Gamma(s) = \frac{1}{h_\tau}\frac{a_{\text{Booth}}\sin s\cos s}{1+(\frac{a_{\text{Booth}}}{b_{\text{Booth}}})^2\cos^2 s} \tag{13}$$

We define our reference curve to lie centered on the horizon. However, during flight, we rotate the curve by ψ_0 to assist with power generation. Thus the tracking curve used during flight is given by

$$\Gamma(s,\psi_0) = \underbrace{\begin{bmatrix} \cos(\psi_0) & 0 & -\sin(\psi_0) \\ 0 & 1 & 0 \\ \sin(\psi_0) & 0 & \cos(\psi_0) \end{bmatrix}}_{\mathbf{M}_{\text{WP}}} \Gamma_P(s) \tag{14}$$

Finally, the tangent of the curve is given by $\mathbf{t}(s) = \frac{d\Gamma}{ds} = \frac{\partial\Gamma}{\partial\lambda_\Gamma}\frac{\partial\lambda_\Gamma}{\partial s} + \frac{\partial\Gamma}{\partial\phi_\Gamma}\frac{\partial\phi_\Gamma}{\partial s}$.

As shown in Fig. 7, the shortest path from the position of the aircraft (denoted by $\mathbf{K}$) to the closet point on the tracking curve (denoted by $\mathbf{C}$), is given by the geodesic vector $\boldsymbol{\sigma}$. For perfect path tracking, we need to minimize $||\boldsymbol{\sigma}||_2$. Taking the shortest path, however, would result in the aircraft intercepting the curve perpendicularly. In practice, this is not desirable and thus we need to introduce a commanded flight direction that results in the distance to the tracking curve being minimized, while also ensuring that when the aircraft intercepts the tracking curve, its kinematic velocity is

aligned with the tangent of the curve, $\mathbf{t}$.

The commanded flight path can be defined on $\mathbb{S}^2$, independently of the distance to the origin by simply scaling the parameters a_{Booth} and b_{Booth} by $1/h_\tau$. The optimal course angle $(\chi)_\tau$ should point the aircraft along the geodesic when far from the curve, however, point perpendicular to the geodesic to align with $\mathbf{t}(s)$ when close to the curve. To remain on the tracking sphere, the optimal flight path angle is set to zero.

To this end, let us define the optimal course and path angles as

$$(\gamma_{\text{cmd}})_\tau = 0, \quad (\chi_{\text{cmd}})_\tau = (\chi_\parallel)_\tau + (\Delta\chi)_\tau \tag{15}$$

with $(\chi_\parallel)_\tau = \arctan \frac{t_y}{t_x}$, where t_x and t_y denote the x and y components of the curve tangent. The second component, $\Delta\chi_\tau$, of the command course angle ensures that as we approach the tracking curve, we align ourselves with the curve tangent $\mathbf{t}$. This is done by introducing a tuning parameter δ_0, allowing us to calculate course change as

$$(\Delta\chi)_\tau = \arctan \frac{\text{sign}(\sigma)||\boldsymbol{\sigma}||_2}{\delta_0} \tag{16}$$

This tracking strategy is visualized in Fig. 4 and will be used to define the target set during the reachability calculation in Section IV.

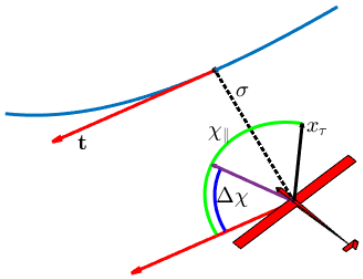

Fig. 4 Visualization of the guidance strategy to produce the optimal course heading (purple arrow).

III. Model Abstraction and Safety Considerations

For the derivation of the safety controller presented in Section IV, the previously introduced model does not suffice, since it requires too many states for synthesis. We thus begin by introducing a simplification of the tether model that allows us to introduce adversarial winch control into the AWE dynamics. Together with a new reference frame and the subsequent safety control model, this section provides the first of our four key contributions.

A. Simplified Tether Model

As mentioned in the previous sections, a full particle tether model requires too many states, prohibiting its adoption for the safety controller. Initial attempts at using simplified tether approximations, such as those derived in [11, 13, 37, 38], were found to be insufficient for safety-control synthesis of fixed wing aircraft as the assumption of the aircraft maintaining aerodynamic equilibrium is not necessarily valid during the avoidance maneuver. Thus an alternative approach to simplifying the complex tether model is introduced.

From field tests conducted with an aircraft in [25], for a small aircraft the tether forces far exceed the gravitational forces and a straight tether approximation is reasonable. However, if larger systems with larger tethers are employed, the tether sag will need to be taken into account. For the AWE system considered in this paper, for the purpose of controller synthesis, we assume that the tether sag remains negligible and, therefore, opt to approximate the position and velocity of the tether segments. To this end, we assume that the position and velocity of the tether segments are distributed evenly along a straight line between the origin and the position of the aircraft. Thus the tether particle's position and velocity can be computed as the x, y, and z projections of the straight tether up to the i-th particle, i.e.,

$$\mathbf{p}_i = \frac{i h_\tau}{n+1} \begin{bmatrix} \cos(\phi)\cos(\lambda) \\ \cos(\phi)\sin(\lambda) \\ \sin(\phi) \end{bmatrix} \tag{17}$$

$$\mathbf{v}_i = \frac{i \dot{h}_\tau}{n+1} \begin{bmatrix} \cos(\phi)\cos(\lambda) \\ \cos(\phi)\sin(\lambda) \\ \sin(\phi) \end{bmatrix} - \frac{i h_\tau}{n+1} \begin{bmatrix} \sin(\phi)\dot{\phi}\cos(\lambda) + \cos(\phi)\sin(\lambda)\dot{\lambda} \\ \sin(\phi)\dot{\phi}\sin(\lambda) - \cos(\phi)\cos(\lambda)\dot{\lambda} \\ -\cos(\phi)\dot{\phi} \end{bmatrix} \tag{18}$$

In Fig. 3 a comparison of the straight tether and the full tether model is shown. Recall that the tether force acting on the aircraft is given by the spring force of the (n+1)-th segment, i.e., $\mathbf{F}_t = \mathbf{F}_{s,n+1}$. The dominating factor in Hooke's law is given by the term $||\mathbf{s}_{n+1}||_2 - l_s$, which is the difference between the segment length and the distance between the final tether point mass and the aircraft. Having $||\mathbf{s}_{n+1}||_2 - l_s > 0$ implies the distance is greater than the length of the tether and thus the tether is under tension. A similar approach of modeling the tether by considering the effect of the tether elongation as the dominant term was recently also presented in [29]. However, in contrast to [29], for the proposed fixed-wing aircraft the damping term is not considered negligible. Modeling this term accurately is imperative for calculating the tether force, as the slightest deviations result in vastly inaccurate force calculations. To this end, let us introduce $\Delta_t = ||\mathbf{s}_{n+1}||_2 - l_s$ as an additional state. By (9), the tether force acting on the aircraft can be calculated as

$$\mathbf{F}_t = \left(k\Delta_t + c\left(\frac{\mathbf{s}_{n+1}}{||\mathbf{s}_{n+1}||_2}\mathbf{s}_{v,n+1}\right)\right)\frac{\mathbf{s}_{n+1}}{||\mathbf{s}_{n+1}||_2} \tag{19}$$

where the position and velocity of the tether point masses is computed using (18). Since we wish to consider an upper bound on the tether force, we utilize an upper bound for the damping and stiffness coefficients based on the minimum expected tether segment length. This reduces complexity while adding robustness to uncertainty in the measured Δ_t.

The derivative of Δ_t is given by

$$\dot{\Delta}_t = \frac{\mathbf{s}_{v,n+1}^T \mathbf{s}_{n+1}}{||\mathbf{s}_{n+1}||_2} - \frac{\dot{l}_s}{n+1} \tag{20}$$

In order to keep the number of system states minimal, we need to decouple the winch system from the aircraft dynamics. To this end, we model the effects of the winch as a scalar disturbance, $d_{\Delta_t} := \dot{\Delta}_t$. By accounting for a worst-case winch behavior, the system can be considered robust to arbitrary winch control. To compute the expected range of values that the derivative of Δ_t might take, we can consider the winch control strategy and derive bounds on the maximum/minimum reeling speed. However, to translate the bounds on the reeling speed to bounds on the derivative of Δ_t, we require also bounding the term $\mathbf{s}_{v,n+1}$. This would result in a coupling between the wind disturbance and the disturbances desired to model adversarial effects on Δ_t. Since combing the worst-case $\mathbf{s}_{v,n+1}$ with the worst-case $\dot{l}_s$, also leads to overly conservative bounds on $\dot{\Delta}_t$, an alternative empirical approach was adopted whereby the bounds are computed by means of simulation. To this end, we measure $\dot{\Delta}_t$ during flight as shown in Fig. 5. Determining the bounds on $\dot{\Delta}_t$ utilizing flight data could be employed while providing probabilistic guarantees for safety with a high degree of confidence, by utilizing methods such as the scenario approach [39]. Incorporating probabilistic confidence bounds is beyond the scope of the work, however, further motivates the empirical approach to estimating $\dot{\Delta}_t$.

As shown in Fig. 5, since $\dot{\Delta}_t$ never exceeds $0.0015\frac{m}{s}$, we constrain the disturbance, d_{Δ_t}, to lie within the interval $[-d_{\Delta_t,\max}, d_{\Delta_t,\max}]$ with $d_{\Delta_t,\max} = 0.005\frac{m}{s}$.

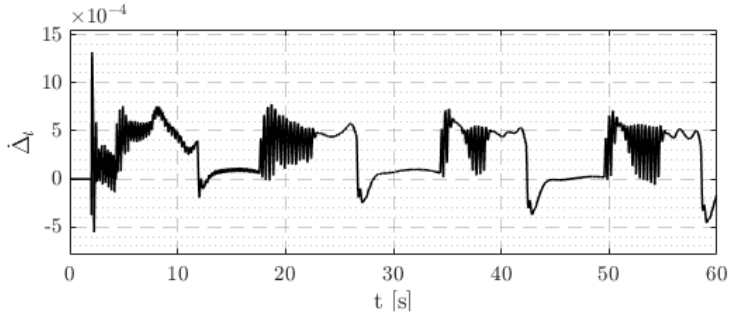

Fig. 5 $\dot{\Delta}_t$ during the traction phase of flight, using the primary path-following controller.

B. Adversarial Wind Turbulence

Since we model the wind turbulence as a stochastic process, we need to ensure that the safety controller can account for worst-case wind gusts, i.e., wind gusts that drive the system away from its target trajectory, and/or lead to a tether rupture. To this end, we model the wind turbulence as an adversarial disturbance input to the system. Thus the wind

velocity for controller synthesis is given by

$$(\mathbf{v}_W)_O = (\mathbf{v}_{shear})_O + (\mathbf{d}_{turb})_O \tag{21}$$

where $\mathbf{d}_{turb} \in \mathbb{R}^3$ is an additional disturbance vector. Similarly, any uncertainty in the wind shear can be included in this additive disturbance and will therefore not be treated separately.

In the same manner that we computed the bounds for d_{Δ_t}, we simulate the flight of the aircraft using the primary path-following controller and analyze the behavior of the longitudinal, u_g, lateral, v_g, and vertical, w_g, turbulence velocity aligned along the horizontal relative mean wind vector, as shown in Fig. 6. From the behaviour u_g, v_g and w_g, we can safely choose each element of $\mathbf{d}_{turb}$ to be bounded by $\pm 4\frac{m}{s}$. To achieve these bounds in practice, we can use data-driven approaches with an appropriate estimator [30, 40, 41].

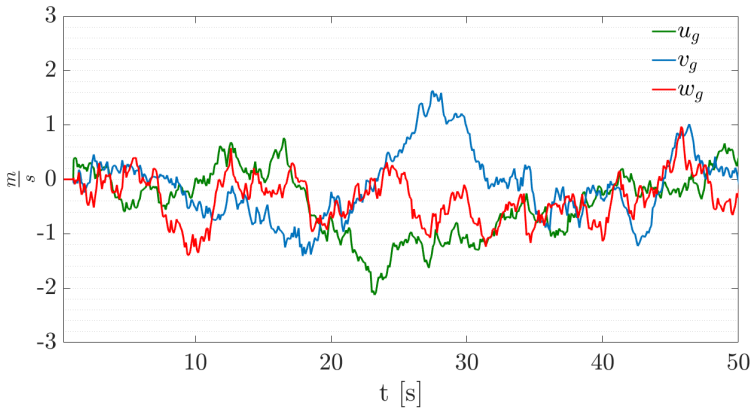

Fig. 6 The behavior of the wind gusts during 50 seconds of flight.

C. Γ Frame and Safety Control Model

As visualized in Fig. 7, the geodesic vector pointing from **C** along the geodesic towards **K**, is always orthogonal to **t**. The derivative of Γ together with the direction of the geodesic vector can, therefore, be used as basis vectors to construct another reference frame that will become useful during gridding, as discussed in Section IV. This new reference frame will be referred to as the Γ frame. Any point on $\mathbb{S}^2$ defined using the longitude, λ, and latitude, ϕ, can also be defined using the Γ frame, where the first coordinate, s, describes an arbitrary point along the curve Γ, and the second coordinate $\sigma = ||\boldsymbol{\sigma}||_2$ describes the geodesic distance in meters perpendicular to $\mathbf{t}(s)$. The calculation of the geodesic for a sphere is derived from [42, pg. 216] and relies on solving the geodesic equations for a sphere.

The derivatives of s can be obtained by projecting the kinematic velocity of the aircraft onto **t**. Similarly, the

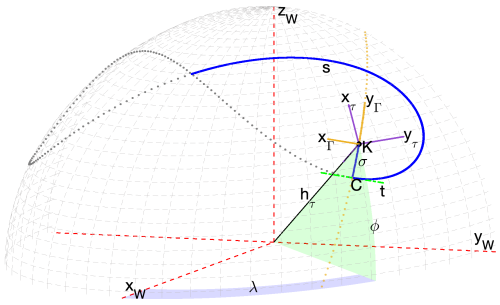

Fig. 7 Visualization of the Γ frame. s is used to denote the position along the reference curve. The geodesic vector, σ, describes the distance to the reference curve.

derivative of σ is obtained by projecting the kinematic velocity onto a perpendicular rotation of $\mathbf{t}$, denoted by $\mathbf{t}_\perp$.

$$\dot{s} = \frac{(\mathbf{t})_\tau (\mathbf{v}_k)_\tau}{||\mathbf{t}||_2 l_\Gamma} \tag{22}$$

$$\dot{\sigma} = \frac{(\mathbf{t}_\perp)_\tau (\mathbf{v}_k)_\tau}{||\mathbf{t}_\perp||_2} \tag{23}$$

where l_Γ denotes the arc length of the Lissajous curve Γ. Using the Γ frame allows us to replace the longitude and latitude resulting in the final set of states used for controller synthesis

$$\mathbf{x} := [s, \sigma, h_\tau, v_\mathrm{a}, \chi_\mathrm{a}, \gamma_\mathrm{a}, \Delta_t]^T \in \mathbb{R}^7 \tag{24}$$

The transformation between the NED frame and the Γ frame is not bijective, thus we need to take the velocity vectors into account to derive a deterministic transformation. To this end, we choose the transformation from the NED frame to the Γ frame, such that the error between $(\mathbf{v}_\mathrm{k})$ and $\mathbf{t}$ is minimized. Finally, we can summarize the equations of motion for the simplified aircraft model as $\dot{\mathbf{x}} = \mathbf{f}(\mathbf{x}, \mathbf{u}, \mathbf{d})$. The control inputs, $\mathbf{u}$, and disturbances, $\mathbf{d}$, are defined as

$$\mathbf{u} := \begin{bmatrix} \alpha_\mathrm{a} \\ \mu_a \end{bmatrix} \in U \subset \mathbb{R}^2, \quad \mathbf{d} := \begin{bmatrix} d_{\Delta_t} \\ \mathbf{d}_\mathrm{turb} \end{bmatrix} \in D \subset \mathbb{R}^4 \tag{25}$$

The aircraft dynamics are composed of $\hat{\mathbf{f}}$, affected only by the control inputs, and $\mathbf{f}_C(\mathbf{x}, \mathbf{d})$, affected only by the disturbances and incorporating all remaining additive terms, i.e., $\mathbf{f}(\mathbf{x}, \mathbf{u}, \mathbf{d}) = \hat{\mathbf{f}}(\mathbf{x}, \mathbf{u}) + \mathbf{f}_C(\mathbf{x}, \mathbf{d})$. If the disturbance does not appear in the dynamics in an affine manner [43, pg. 133], the reachability problem remains solvable, however, a numerical minimizer of the Hamiltonian might become necessary (e.g., by gridding the domain of the control inputs). Since this usually impedes on computational complexity, utilizing the structure to develop analytic expressions for the optimizers is beneficial.

Decomposing the dynamics serves both the presentation of the final system dynamics, as well as the derivation

of the Hamiltonian in the subsequent section. Since the control inputs affect only the aircraft velocity, course, and path angles, with a slight abuse of notation, we omit the four remaining state derivatives that are zero, allowing us to summarize $\hat{\mathbf{f}}(\mathbf{x}, \mathbf{u})$ as

$$\hat{\mathbf{f}}(\mathbf{x}, \mathbf{u}) = \frac{1}{m_\mathrm{a}} \begin{bmatrix} 1 & 0 & 0 \\ 0 & \frac{1}{v_\mathrm{a} \cos \gamma_\mathrm{a}} & 0 \\ 0 & 0 & -\frac{1}{v_\mathrm{a}} \end{bmatrix} \mathbf{M}_{\overline{\mathrm{A}}\mathrm{A}} \mathbf{M}_{\mathrm{AB}} (\mathbf{F}_\mathrm{a})_\mathrm{B} \tag{26}$$

The term $\mathbf{f}_C(\mathbf{x}, \mathbf{d})$ is then given by

$$\mathbf{f}_C(\mathbf{x}, \mathbf{d}) = \underbrace{\left[\frac{(\mathbf{t})_\tau (\mathbf{v}_k)_\tau}{||\mathbf{t}||_2 l_\Gamma},\ \frac{(\mathbf{t}_\perp)_\tau (\mathbf{v}_k)_\tau}{||\mathbf{t}_\perp||_2},\ -(v_\mathrm{k})_{\tau,\mathrm{z}},\ \frac{(F_\mathrm{t})_{\overline{\mathrm{A}},x}}{m_\mathrm{a}},\ \frac{(F_\mathrm{t})_{\overline{\mathrm{A}},y}}{m_\mathrm{a} v_\mathrm{a} \cos \gamma_\mathrm{a}},\ -\frac{(F_\mathrm{t})_{\overline{\mathrm{A}},z}}{m_\mathrm{a} v_\mathrm{a}},\ 0 \right]^T}_{=\mathbf{f}_{C1}(\mathbf{x}, \mathbf{d}_\mathrm{turb})} \tag{27}$$

$$+ \underbrace{\left[0,\ 0,\ 0,\ 0,\ 0,\ 0,\ d_{\Delta_t} \right]^T}_{=\mathbf{f}_{C2}(\mathbf{x}, d_{\Delta_t})} \tag{28}$$

$$+ \underbrace{\left[0,\ 0,\ 0,\ \frac{(F_\mathrm{g})_{\overline{\mathrm{A}},x}}{m_\mathrm{a}},\ \frac{(F_\mathrm{g})_{\overline{\mathrm{A}},y}}{m_\mathrm{a} v_\mathrm{a} \cos \gamma_\mathrm{a}},\ -\frac{(F_\mathrm{g})_{\overline{\mathrm{A}},z}}{m_\mathrm{a} v_\mathrm{a}},\ 0 \right]^T}_{=\mathbf{f}_{C3}(\mathbf{x})} \tag{29}$$

where we adopt the same notation as before to denote the x, y, and z components of the forces in the $\overline{\mathrm{A}}$ frame and simplify the notation by omitting the dependence of $\mathbf{d}_\mathrm{turb}$ and $\mathbf{x}$ in the tether and gravitational forces.

IV. HJ Reachability Analysis and Controller Synthesis

A. Problem Statement

Having formulated the system dynamics, we are able to introduce the necessary concepts of HJ reachability analysis used for controller synthesis. The synthesized controller and subsequent hybrid control laws provide the second key contribution of this paper.

Let $\mathcal{R}$ be the reach set, the set of states that should be reached in a given time, and let $\mathcal{A}$ be the set of avoid states, the set of states that lead to a critical system failure (i.e., tether rupture). Then we can define the backward reachable set (BRS) as the set of states from which it is possible to reach the set $\mathcal{R}$ at the end of a given time interval with duration T while guaranteeing never to enter the set $\mathcal{A}$ until then. Mathematically, let $\mathbf{x} \in \mathbb{R}^7$ be the system state defined in (24) evolving according to the ordinary differential equation

$$\dot{\mathbf{x}}(t) = \mathbf{f}(\mathbf{x}(t), \mathbf{u}(t), \mathbf{d}(t)), \quad t \in [-T, 0], \mathbf{u} \in \mathcal{U}, \mathbf{d} \in \mathcal{D} \tag{30}$$

Note that we treat time as negative consistent with [19, 44]; this only simplifies some of the notation and implies that we start our system at time $-T$. The dynamics, $\mathbf{f}$, are assumed to be bounded and Lipschitz continuous in $\mathbf{x}$ and uniformly continuous in $\mathbf{u}$ and $\mathbf{d}$. Then, given the Lebesgue-measurable functions $\mathbf{u}(\cdot) \in \mathcal{U}$ and $\mathbf{d}(\cdot) \in \mathcal{D}$, the control and disturbance inputs, respectively, there exists a unique trajectory, $\boldsymbol{\zeta}$, solving (30), i.e.,

$$\frac{\partial}{\partial t}\boldsymbol{\zeta}(t; \mathbf{x}_0, \mathbf{u}(\cdot), \mathbf{d}(\cdot)) = \mathbf{f}(\boldsymbol{\zeta}(t; \mathbf{x}_0, \mathbf{u}(\cdot), \mathbf{d}(\cdot)), \mathbf{u}(t), \mathbf{d}(t)) \; \forall t \in [-T, 0]$$
$$\boldsymbol{\zeta}(-T; \mathbf{x}_0, \mathbf{u}(\cdot), \mathbf{d}(\cdot)) = \mathbf{x}_0$$

To capture the worst-case disturbance, we model the underlying control problem as a differential game of two players. Following [45], we restrict the first player to play a nonanticipative strategy [46, 47], which is a function $\boldsymbol{\xi} : \mathcal{D} \to \mathcal{U}$, such that for all $t \in [-T, 0]$ and for all $\mathbf{d}, \hat{\mathbf{d}} \in \mathcal{D}$, if $\mathbf{d}(\tau) = \hat{\mathbf{d}}(\tau)$ for almost every $\tau \in [-T, t]$, then $\boldsymbol{\xi}[\mathbf{d}](\tau) = \boldsymbol{\xi}[\hat{\mathbf{d}}](\tau)$ for almost every $\tau \in [-T, t]$. Furthermore, we use Σ to denote the class of nonanticipative strategies.

Finally, we can define the BRS as

$$\text{BRS}_{\mathcal{A},\mathcal{R}}(-T) = \left\{\mathbf{x} \in \mathbb{R}^7 | \exists \boldsymbol{\xi}(\cdot) \in \Sigma, \forall \mathbf{d}(\cdot) \in \mathcal{D}, (\boldsymbol{\zeta}(0; \mathbf{x}, \boldsymbol{\xi}(\cdot), \mathbf{d}(\cdot)) \in \mathcal{R}) \;\&\; (\forall \tau \in [-T, 0], \boldsymbol{\zeta}(\tau; \mathbf{x}, \boldsymbol{\xi}(\cdot), \mathbf{d}(\cdot)) \notin A)\right\} \quad (31)$$

In words, $\text{BRS}_{\mathcal{A},\mathcal{R}}(-T)$ is the set of states from which trajectories can start at $-T$, and there exists a choice for a non-anticipative strategy $\boldsymbol{\xi}$, such that for any disturbance strategy $\mathbf{d}$, the system state can reach $\mathcal{R}$ at the end of the horizon while avoiding $\mathcal{A}$ until then.

By defining the avoid states as the set of states that imply a tether rupture, and the reach set as the set of states that follow the optimal guidance strategy, the BRS is able to provide information about an impending critical failure. Furthermore, by computing the BRS, we are able to simultaneously find the optimal trajectory and control policy that allows for optimal flight while avoiding critical states.

Recall that the maximum force acting on the tether is given by the final segment attached to the aircraft. Thus, by setting the maximum allowed tether force as F_{rupture}, we can define the Lipschitz continuous function $h(\mathbf{x}) = ||\mathbf{F}_t||_2 - F_{\text{rupture}}$. Then we can define the avoid set related to the superzero level-set of $h(\cdot)$ as $\mathcal{A} = \{\mathbf{x} \in \mathbb{R}^7 | h(\mathbf{x}) > 0\}$.

Rather than defining our target set $\mathcal{R}$ as being the set of states that lie on the optimal tracking curve, we define our target set as all states that are aligned with the commanded flight direction. To this end, we can define Lipschitz continuous function $l(\cdot)$ by taking the signed distance functions of the course and path errors in the NED frame. Since the primary objective of the safety maneuver is not optimal path following, but rather the avoidance of the tether rupture, the target set should simply favor the commanded course and path angles, rather than strictly enforcing equality. This is done by introducing a tolerance $\epsilon > 0$. The resulting signed distance function is $l(\mathbf{x}) = \max\{|\gamma_{\text{cmd},O} - (\gamma)_O|, |\chi_{\text{cmd},O} - (\chi)_O|\} - \epsilon$, where $(\gamma)_O$ and $(\chi)_O$ are the 5th and 6th states of our system transformed to the NED frame. The reach set is then

defined by the subzero level-set of $l(\cdot)$, i.e., $\mathcal{R} = \{\mathbf{x} \in \mathbb{R}^7 | l(\mathbf{x}) \leq 0\}$.

Using the definition of $\mathcal{A}$ and $\mathcal{R}$, as in [45], it can be shown that $\text{BRS}_{\mathcal{A},\mathcal{R}}(-T) = \{\mathbf{x} \in \mathbb{R}^7 | V(\mathbf{x}, T) \leq 0\}$, where

$$V(\mathbf{x}, t) = \inf_{\boldsymbol{\xi}(\cdot)\in\Sigma} \sup_{\mathbf{d}(\cdot)\in\mathcal{D}} \max \left\{ l(\boldsymbol{\zeta}(0; \mathbf{x}, \boldsymbol{\xi}(\cdot), \mathbf{d}(\cdot)), \max_{\tau\in[-t,0]} h(\boldsymbol{\zeta}(\tau; \mathbf{x}, \boldsymbol{\xi}(\cdot), \mathbf{d}(\cdot)) \right\} \tag{32}$$

Furthermore, as in [45], the value function in (32) is the unique continues viscosity solution of the following quasi-variational inequality

$$\max \left\{ h(\mathbf{x}) - V(\mathbf{x}, t), \frac{\partial V(\mathbf{x}, t)}{\partial t} + \sup_{\mathbf{d}\in D} \inf_{\mathbf{u}\in U} \frac{\partial V(\mathbf{x}, t)}{\partial \mathbf{x}} f(\mathbf{x}, \mathbf{u}, \mathbf{d}) \right\} = 0 \tag{33}$$

with terminal condition $V(\mathbf{x}, 0) = \max\{h(\mathbf{x}), l(\mathbf{x})\}$ and where D and U are the compact sets of possible disturbance and control inputs, respectively as defined in (25). For numerical reasons, it has become common practice to solve (33) using level-set methods in combination with upwinding schemes such as essential non-oscillatory schemes [48]. Alternative methods for solving (33), such as using Deep Learning [49] have been proposed, however, they lack many of the performance and safety guarantees we require.

To apply level-set methods to (33), we are required to grid the state space, thus exponentially scaling the memory requirements with each additional state. This necessitates the need for the low dimensional model of the AWE system derived earlier in Section III. Furthermore, for each grid node, we are required to evaluate the dynamics and calculate the derivative of the value function. Therefore, to minimize computational overhead, we need to ensure we only consider grid nodes that are relevant during flight. To use conventional level-set methods, however, we are required to use an evenly spaced grid. As can be seen in Fig. 8, gridding the position of the aircraft in the NED frame is inefficient compared to the new Γ frame introduced in Section III.C.

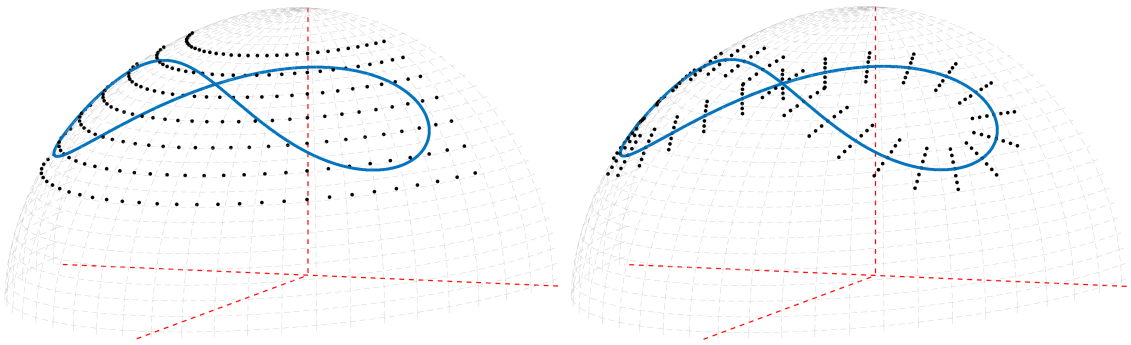

Fig. 8 Comparison of a 31×7 grid in the NED frame vs the Γ frame. The Γ frame successfully captures only relevant nodes close to the optimal tracking curve.

B. Optimal Control and Disturbance Inputs

To solve (33), we are required to find the optimal control and disturbance inputs that are the minimizers and maximizers, respectively, of $\sup_{\mathbf{d}\in D}\inf_{\mathbf{u}\in U}\frac{\partial V(\mathbf{x},t)}{\partial x}\mathbf{f}(\mathbf{x},\mathbf{u},\mathbf{d})$. To this end let us define the Hamiltonian of the system as

$$H(\mathbf{x},\mathbf{q}) = \max_{\mathbf{d}\in D}\min_{\mathbf{u}\in U}\mathbf{q}^T\mathbf{f}(\mathbf{x},\mathbf{u},\mathbf{d}) \tag{34}$$

where $\mathbf{q} = [q_1,\ldots,q_7] \in \mathbb{R}^7$ is the costate vector and since both D and U are compact, we are able to define the Hamiltonian using the max and min over D and U, instead of the sup and inf, respectively, i.e., the optimizers are achieved. To determine the optimizers in (34) we utilize the separation of the dynamics presented in Section III.C. This allows us to write the Hamiltonian as

$$H(\mathbf{x},\mathbf{q}) = \min_{\mathbf{u}\in U}\mathbf{q}^T\hat{\mathbf{f}}(\mathbf{x},\mathbf{u}) + \max_{\mathbf{d}\in D}\mathbf{q}^T\mathbf{f}_C(\mathbf{x},\mathbf{d}) \tag{35}$$

separating the control from the disturbance inputs. We begin by finding the control inputs that minimize the Hamiltonian

$$\mathbf{u}^* \in \arg\min_{\mathbf{u}\in U}\mathbf{q}^T\hat{\mathbf{f}}(\mathbf{x},\mathbf{u}) = \arg\min_{\mathbf{u}\in U}\frac{1}{m_\mathrm{a}}\begin{bmatrix} q_4 & \frac{q_5}{v_\mathrm{a}\cos\gamma_\mathrm{a}} & -\frac{q_6}{v_\mathrm{a}}\end{bmatrix}\mathbf{M}_{\overline{\mathrm{A}}\mathrm{A}}(\mu)\mathbf{M}_{\mathrm{AB}}(\alpha,\beta)(\mathbf{F}_\mathrm{a}(\alpha,v_a))_\mathrm{B} \tag{36}$$

Since the derived avoidance maneuver needs to adhere to control constraints placed on the path-following controller, notably limiting the range of bank angles, no analytic expression for (36) could be found. However, since we only need to know the optimal control inputs for a finite number of v_a, γ, q_4, q_5, and q_6 values, we grid the input space and evaluate (36) for discrete values of μ and α to find the near-optimal control inputs, i.e.,

$$\mathbf{u}^* \in \underset{\alpha\in[\alpha_1,\ldots,\alpha_n],\mu\in[\mu_1,\ldots,\mu_m]}{\arg\min} v_\mathrm{a}q_4(a(\alpha)\cos(\alpha)+b(\alpha)\sin(\alpha)) + (\frac{q_5}{\cos\gamma_\mathrm{a}}\sin(\mu)+q_6\cos(\mu))(b(\alpha)\cos(\alpha)-a(\alpha)\sin(\alpha)) \tag{37}$$

where $a(\alpha)$ and $b(\alpha)$ are second order polynomials and $[\alpha_0,\ldots,\alpha_n]$ and $[\mu_1,\ldots,\mu_m]$ are discrete values of α and μ, respectively. Notice that u^* is a state-feedback controller as it depends on the state implicitly through the costate vector q.

Determining the control inputs that minimize the Hamiltonian by means of (37), we proceed to find the worst-case disturbances as the maximizer of the Hamiltonian, i.e., $\mathbf{d}^* \in \arg\max_{\mathbf{d}\in D}\mathbf{q}^T\mathbf{f}_C(\mathbf{x},\mathbf{d}) = \arg\max_{d_{\Delta_t},\mathbf{d}_\mathrm{turb}}\mathbf{q}^T(\mathbf{f}_{C1}(\mathbf{x},\mathbf{d}_\mathrm{turb}) + \mathbf{f}_{C2}(\mathbf{x},d_{\Delta_t}))$ Due to this separable structure, we begin by computing the worst-case disturbance, d_{Δ_t}, which captures adverser winch control

$$d^*_{\Delta_t} \in \underset{d_{\Delta_t}\in[-d_{\Delta_t,\max},d_{\Delta_t,\max}]}{\arg\max}\mathbf{q}^T\mathbf{f}_{C2}(\mathbf{x},d_{\Delta_t}) \tag{38}$$

where $d_{\Delta_t,\max} = 0.005$ is considered the bound of $\dot{\Delta}_t$ as derived in Section III.A. Solving (38) yields $d^*_{\Delta_t} =$

$-\text{sign}(q_7)d_{\Delta_t,\max}$.

For the computation of the disturbance vector $\mathbf{d}_{\text{turb}}$, the worst-case wind turbulence, we need to consider the effects the wind turbulence has on the position and heading of the aircraft. The wind turbulence naturally influences the wind velocity (21) and subsequently the kinematic velocity of the aircraft (2). We thus begin by rewriting the kinematic velocity in the τ frame, whereby we replace the wind turbulence with the disturbance vector $\mathbf{d}_{\text{turb}}$, i.e.,

$$(\mathbf{v}_{\text{k}})_\tau = \underbrace{\mathbf{M}_{\tau\text{W}}\mathbf{M}_{\text{WO}}\left(\mathbf{M}_{\text{O}\overline{\text{A}}}\begin{bmatrix} v_{\text{a}} \\ 0 \\ 0 \end{bmatrix}_{\overline{\text{A}}} + (\mathbf{v}_{\text{shear}})_{\text{O}}\right)}_{(\mathbf{v}_{\text{k},0})_\tau} + \underbrace{\mathbf{M}_{\tau\text{W}}(\mathbf{d}_{\text{turb}})_{\text{W}}}_{(\mathbf{d}_{\text{turb}})_\tau} \tag{39}$$

This allows us to rewrite the position propagation in the NED frame as

$$\dot{\lambda} = \underbrace{\frac{(v_{\text{k},0})_{\tau,\text{y}}}{\cos(\phi)h_\tau}}_{\dot{\lambda}_0} + \frac{(d_{\text{turb}})_{\tau,\text{y}}}{\cos(\phi)h_\tau}, \quad \dot{\phi} = \underbrace{\frac{(v_{\text{k},0})_{\tau,\text{x}}}{h_\tau}}_{\dot{\phi}_0} + \frac{(d_{\text{turb}})_{\tau,\text{x}}}{h_\tau}, \quad \dot{h}_\tau = \underbrace{-(v_{\text{k},0})_{\tau,\text{z}}}_{\dot{h}_{\tau,0}} - (d_{\text{turb}})_{\tau,\text{z}} \tag{40}$$

where $(v_{\text{k},0})_{\tau,\text{x}}$, $(v_{\text{k},0})_{\tau,\text{y}}$ and $(v_{\text{k},0})_{\tau,\text{z}}$ denote the x, y, and z components of the base kinematic velocity in the τ frame and $(d_{\text{turb}})_{\tau,\text{x}}$, $(d_{\text{turb}})_{\tau,\text{y}}$ and $(d_{\text{turb}})_{\tau,\text{z}}$ denote the x, y, and z components of the turbulence disturbance vector in the τ frame. Recall that the tether force (19) is also affected by the kinematic velocity of the aircraft through the difference between the velocity of the aircraft and the final tether segment, given by $\mathbf{s}_{v,n+1} = \mathbf{v}_{\text{aircraft}} - \mathbf{v}_n$. Thus the turbulence will only affect the tether force if the turbulence acting on $\mathbf{v}_{\text{aircraft}}$ is notably different from that acting on $\mathbf{v}_n$. Since we already incorporate uncertainty in the tether force by means of d_{Δ_t} and d_{Δ_t} is chosen conservatively, we neglect the minimal impact of the wind turbulence on the tether force.

Thus the worst-case turbulence disturbance can be calculated by

$$\mathbf{d}^*_{\text{turb}} \in \underset{\substack{d_{\text{turb,x}} \in D_{\text{turb}}, \\ d_{\text{turb,y}} \in D_{\text{turb}} \\ d_{\text{turb,z}} \in D_{\text{turb}}}}{\arg\max} \begin{bmatrix} q_1, q_2, q_3 \end{bmatrix} \begin{bmatrix} \dot{\lambda}, \dot{\phi}, \dot{h}_\tau \end{bmatrix}^T \tag{41}$$

where $D_{\text{turb}} = [-d_{\text{turb,max}}, d_{\text{turb,max}}]$, with $d_{\text{turb,max}} = 4\frac{m}{s}$, the possible range of turbulence velocities. The results in (40) utilize the disturbance in the τ frame, while we require the final result to be in the wind frame. To this end, we transform $(\mathbf{d}_{\text{turb}})_\tau$ back into the wind frame and drop the additive term $(\mathbf{v}_{\text{k},0})_\tau$, resulting in the final worst-case

turbulence disturbances that maximize the Hamiltonian

$$
\begin{aligned}
d^*_{\text{turb,x}} &= -d_{\text{turb,max}} \cdot \text{sign}\Big[\sin(\phi)\cos(\lambda)(q_1 \frac{(t)_{\tau,\text{x}}}{||\mathbf{t}||_2 l_\Gamma} + q_2 \frac{(t_\perp)_{\tau,\text{x}}}{||\mathbf{t}_\perp||_2}) + \sin(\lambda)(q_1 \frac{(t)_{\tau,\text{y}}}{||\mathbf{t}||_2 l_\Gamma} + q_2 \frac{(t_\perp)_{\tau,\text{y}}}{||\mathbf{t}_\perp||_2}) \\
&\quad + \cos(\phi)\cos(\lambda)(q_1 \frac{(t)_{\tau,\text{z}}}{||\mathbf{t}||_2 l_\Gamma} + q_2 \frac{(t_\perp)_{\tau,\text{z}}}{||\mathbf{t}_\perp||_2} - q_3)\Big] \\
d^*_{\text{turb,y}} &= d_{\text{turb,max}} \cdot \text{sign}\Big[-\sin(\phi)\sin(\lambda)(q_1 \frac{(t)_{\tau,\text{x}}}{||\mathbf{t}||_2 l_\Gamma} + q_2 \frac{(t_\perp)_{\tau,\text{x}}}{||\mathbf{t}_\perp||_2}) + \cos(\lambda)(q_1 \frac{(t)_{\tau,\text{y}}}{||\mathbf{t}||_2 l_\Gamma} + q_2 \frac{(t_\perp)_{\tau,\text{y}}}{||\mathbf{t}_\perp||_2}) \\
&\quad - \cos(\phi)\sin(\lambda)(q_1 \frac{(t)_{\tau,\text{z}}}{||\mathbf{t}||_2 l_\Gamma} + q_2 \frac{(t_\perp)_{\tau,\text{z}}}{||\mathbf{t}_\perp||_2} - q_3)\Big] \\
d^*_{\text{turb,z}} &= d_{\text{turb,max}} \cdot \text{sign}\Big[\cos(\phi)(q_1 \frac{(t)_{\tau,\text{x}}}{||\mathbf{t}||_2 l_\Gamma} + q_2 \frac{(t_\perp)_{\tau,\text{x}}}{||\mathbf{t}_\perp||_2}) - \sin(\phi)(q_1 \frac{(t)_{\tau,\text{z}}}{||\mathbf{t}||_2 l_\Gamma} + q_2 \frac{(t_\perp)_{\tau,\text{z}}}{||\mathbf{t}_\perp||_2} - q_3)\Big]
\end{aligned}
$$

With both the worst-case disturbance and optimal control inputs computed, the Hamiltonian can be calculated. To solve (33) we employ the Level Set Method toolbox of [50] and begin by initializing the value function at $t = 0$ with $V(\mathbf{x}, 0) = \max\{h(\mathbf{x}), l(\mathbf{x})\}$. As we solve the quasi-variational inequality (33), we compute the optimal control inputs that form our control policy $\mathbf{u}(\mathbf{x}, t)$. The evolution of the value function over the time period $[-0.1s, 0s]$ is shown in Fig. 9. Any state in the zero-sublevel set belongs to the BRS, i.e., the set of points that can reach $\mathcal{R}$ while avoiding $\mathcal{A}$ within t units of time.

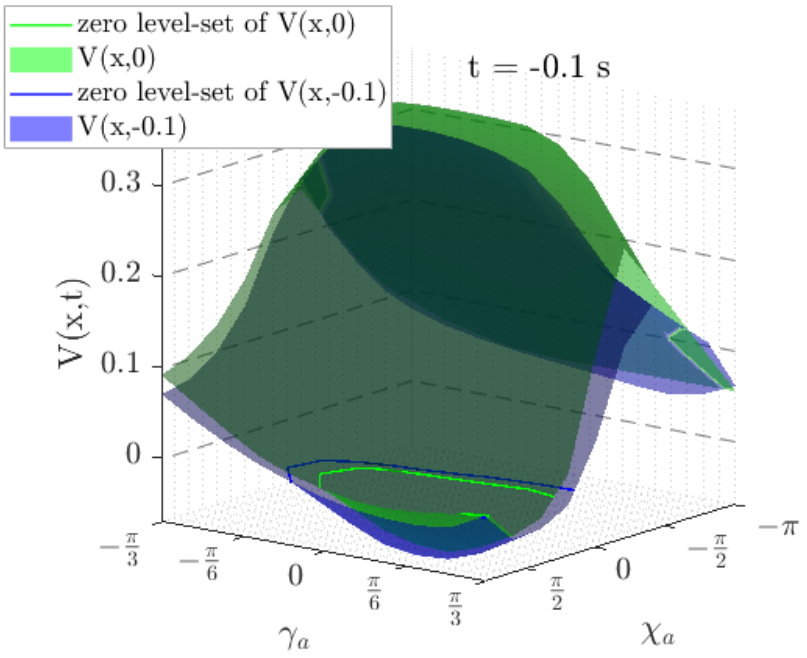

Fig. 9 Visualization of the value function used for safety controller synthesis projected along $[s = 4\pi/3, \sigma = 20m, h_\tau = 250m, v_a = 31m/s, \Delta_t = 0.3mm]$**.**

C. Hybrid Control Setup

Let us refer to the safety and the NDI control laws as u_{safety} and u_{NDI} respectively. The aim is to combine these control laws in such a way as to mitigate the negative effects on power generation through conservative and sub-optimal maneuvers while maintaining safety properties. In the context of flight maneuvers, logic-based switching has become a common practice as it has many advantages over traditional adaptive control techniques, especially when considering systems with a high degree of model uncertainty [43, pg. 75, 130]. Utilizing logic-based switching to incorporate HJ reachability into a least restrictive control law has been demonstrated in the past in [15, 51]. However, unlike previous implementations of the HJ reachability least restrictive control laws, incorporating switching into more complex systems, such as flight control, requires careful consideration of the switching behavior. Badly chosen switching rules can lead to chattering and destabilization of the system. Thus, in summary, we derive a switching law based on the following criteria:

1) Allow for fast switching to the avoidance maneuver to facilitate a rapid response.
2) Prevent the system from being destabilized due to chattering behavior.
3) Account for uncertainty in the tether force estimation.
4) Minimize negative effects on power generation.

A common method to prevent the system from being destabilized is to rely upon slow switching conditions, such as dwell time switching or hysteresis switching. As the avoidance maneuver generated by the safety controller will not have a clear minimum execution time, it becomes difficult to determine the appropriate average dwell time and potential chatter-bound [52]. To this end, the switching law derived in the sequel is designed based on hysteresis switching and sliding modes [43, pg. 12-14]. In the context of systems with large uncertainty, the switching is conventionally performed using supervisory control, whereby an estimator is used in combination with a monitoring signal generator, and finally, a switching logic is used to determine an appropriate controller [43, pg. 133]. The integration of state estimation into the control process is outside the scope of this work, thus we restrict ourselves to deriving an appropriate switching logic.

To create the necessary switching surfaces, we will consider the current tether force as well as a first-order approximation of the predicted tether force. Since the actuation delays are not accounted for in the safety control synthesis, belated switching to the safety controller will potentially not give the safety controller ample time to take the necessary action to avoid a critical system failure. To this end, we choose the switching surface S_1 to lie slightly below the maximum tether rupture force.

$$S_1(\mathbf{F}_t) = (||\mathbf{F}_t||_2 \geq F_{\text{rupture}} - 30N) \quad \vee \quad (||\mathbf{F}_t||_2 + \frac{\partial \overline{||\mathbf{F}_t||}_2}{\partial t} T \geq F_{\text{rupture}} - 50N) \tag{42}$$

where $T = 0.1s$ is the time horizon used for the BRS computation and $\overline{||\mathbf{F}_t||}_2$ is the moving average of the tether force

acting on the aircraft. The numerical values in (42) are tuned experimentally, while due to uncertainty in the linear extrapolation of the tether force, the threshold for the predicted force is chosen lower. As a switch from u_{NDI} to u_{safety} is considered time-sensitive, we utilize sliding modes, to prevent abrupt maneuvers while maintaining speed.

Using solely sliding modes, however, may lead to chattering. To this end, we draw on the aforementioned hysteresis switching logic and define a second switching surface, S_2, that is offset from the first and utilized to switch from u_{safety} to u_{NDI}.

$$S_2(\mathbf{F}_t) = \neg \mathrm{S}_1(||\mathbf{F}_t||_2) \quad \wedge \quad \left[(||\mathbf{F}_t||_2 \leq F_{\text{rupture}} - 40N) \quad \vee \quad (\frac{\partial \overline{||\mathbf{F}_t||_2}}{\partial t} \leq 0)\right] \tag{43}$$

A summary of the switching logic is illustrated in Fig. 10.

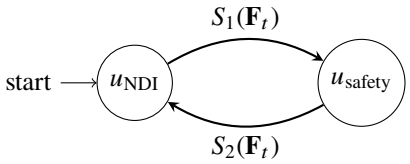

Fig. 10 State automaton of the hybrid control setup.

V. Simulation

A. Simulation Setup

To verify the effectiveness of the derived avoidance strategy, we consider the simplified dynamics derived in III simulated using the worst-case disturbances. As can be seen in Fig. 11, when the avoidance strategy is engaged, the controller derived by means of HJ reachability is successfully able to decrease the tether force. To verify the feasibility of the chosen strategy, however, it is necessary to demonstrate its effectiveness in conjunction with the guidance and regular path-following controllers. Furthermore, integrating the chosen avoidance maneuver into a larger simulation framework serves as validation that the chosen robustness margins are adequate at handling unmodeled adversarial effects, such as actuator delays. To this end, we integrate the avoidance strategy into an extension of the MATLAB Simulink framework presented in [17] and [8].

Together with the subsequent discussion, the validation of the presented hybrid control setup constitutes our fourth key contribution of this paper. Some of the relevant simulation parameters are presented in Table 1 and we have made the simulation code available *.

The aircraft dynamics use the tether force computed by the full tether model as well as the wind velocity computed by the wind field model. To this end, we pass the altitude of the aircraft and the tether segments to the wind field model. Since the aircraft model simulates the dynamics using the τ and the A frame, we need to convert the aircraft's longitude

*https://github.com/nikovert/AWE_Simulation

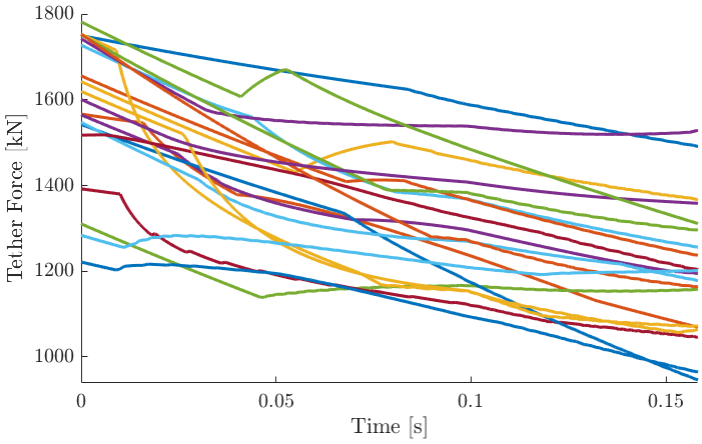

Fig. 11 The tether force acting on the aircraft during the avoidance maneuver under worst-case disturbances. Each color represents a random initial position, velocity, and tether force and the evolution of the tether force as the avoidance maneuver is executed.

Table 1 Simulation Parameters

Parameter	Value	Description
F_{ref}	1600 N	Force tracked by the winch controller
F_{rupture}	1870 N	Force at which a tether rupture occurs
$\|\|W_{20}\|\|$	9 $\frac{m}{s}$	Measured wind speed at 20 feet
ξ	π	Wind direction
n_{tether}	5	Tether segments used during simulation

and latitude to the Γ frame before computing the safety control input. To this end, a guidance model is used, which also provides the pseudo control inputs used by the NDI path following controller.

To acquire the safety control inputs, u_{safety}, we solve (37) using the numerically computed $\frac{\partial V(\mathbf{x},T)}{\partial x}$ as our costate vector. Since calculating the derivatives of the value function is computationally intensive, it is impractical to compute u_{safety} during the simulation. To this end, we calculate the optimal safety control inputs offline using a high fidelity grid and save them on each grid point, using the saved values as a lookup table to be used during simulation.

Both control inputs, u_{safety} and u_{NDI} are passed to the control switch, which determines which control input to use based on the switching law derived in Section IV.C. The final control u_{cmd} is passed to the actuator, which simulates the actuator delays. The bank angle μ_{a} and angle of attack α_{a} are then passed to the aircraft model. To complete the pumping cycle and execute the retraction phase, we utilize the framework derived in [17].

B. Simulation Results

To evaluate the performance of the safety controller, we run the simulation for multiple pumping cycles to determine if at any point, the maximum allowed tether force is exceeded. The tether force of three pumping cycles as well as the switching behavior of the safety controller is shown in Fig. 12, 13 and 14. Notice how the tether force is able to remain

high throughout the pumping cycle and only minimal interventions by the safety controller (blue segments in Fig. 14) are necessary to prevent a tether rupture.

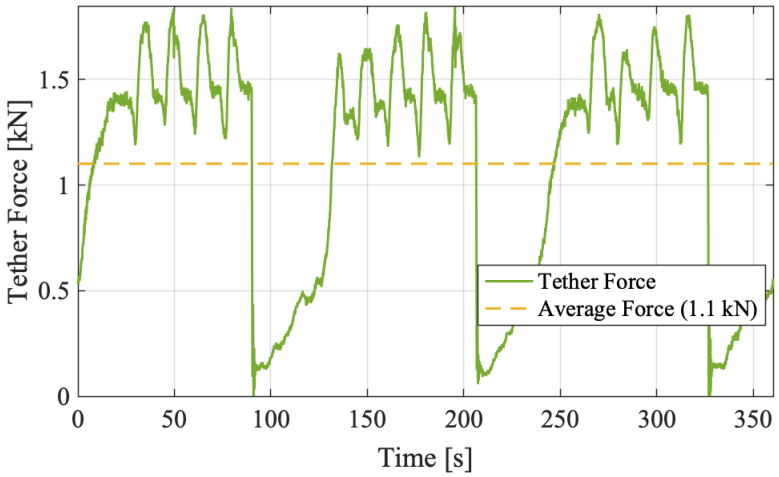

Fig. 12 The tensile force of the tether acting on the aircraft during flight.

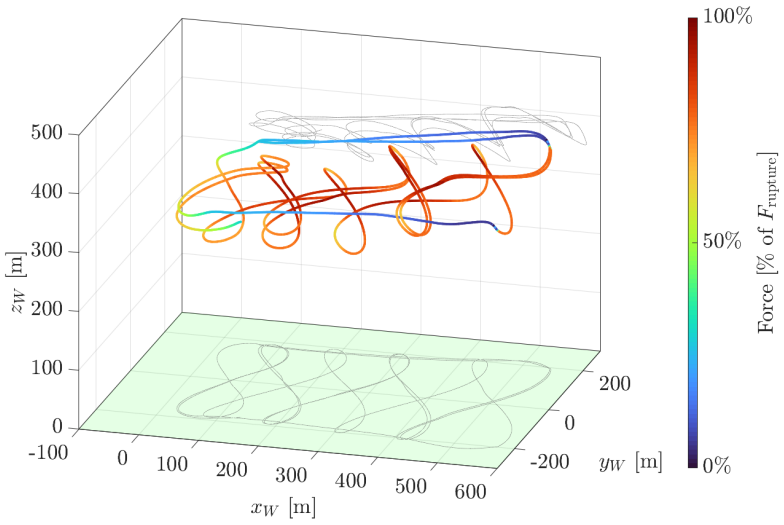

Fig. 13 The tether force in % of the maximum allowed tether force before a rupture occurs.

The mechanical power that is able to by harnessed by the ground station can be calculated by multiplying the tether force at the ground station by the reel-out speed, i.e., $P_{\text{mech}} = \dot{l}_s ||\mathbf{F}_{\text{w}}||_2$. In Fig. 15 and 16, the power generation capabilities of the AWE system are shown. On average the chosen setup is able to produce 3.37 kW of power.

To put the power generation into context, we derive a theoretical upper limit of the power that could be obtained through optimal flight based on the work of [53]. We begin by calculating the maximum power harvesting factor, ζ, based on the drag and lift coefficients presented in [31]. The power harvesting factor is a common metric used by both

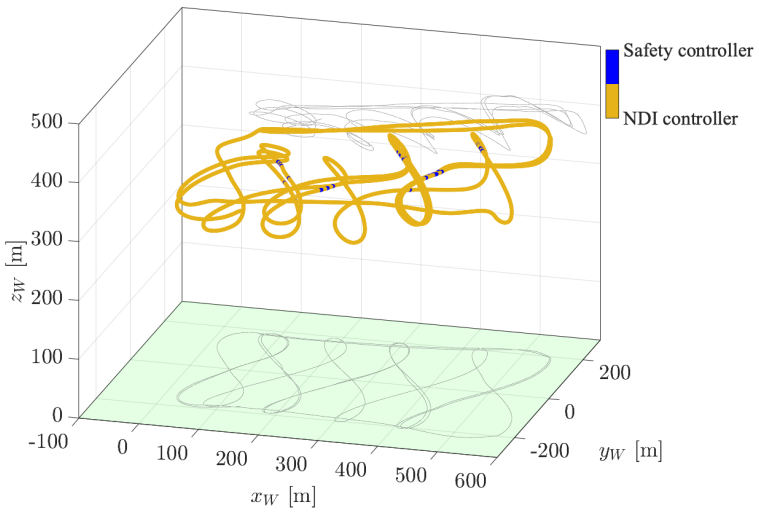

Fig. 14 The safety controller only needs to be activated at particular times. For the remainder of the flight, a more power-optimal controller, such as the NDI controller can be employed.

AWE applications as well as conventional wind turbines (not to be confused with the power coefficient commonly used for wind turbines)

$$\zeta = \frac{4}{27}\frac{C_L^3}{(C_D + C_{D\,\text{tether}})^2} \tag{44}$$

The power harvesting factor is unique for a given AWE setup and is used in [34] and [26] to calculate the theoretical limit P_{max}. However, in order to calculate a tighter, more realistic upper bounds of the power that a given controller could achieve, we calculate an efficiency factor e that can be multiplied by the theoretical upper bound of the power generation, P_{max}. This theoretical upper bound is given by Theorem 1 in [53], $\tilde{P} = P_{\text{max}} \underbrace{\cos^3(\gamma_0)}_{e}$, where γ_0 is the optimal angle between the aerodynamic force and the wind.

Based on the observation that the average aerodynamic force needs to balance the gravitational force acting on the aircraft as well as the force exerted on the aircraft by the tether (assuming that on average the system is not accelerating), we can state the following equality based on a 2-dimensional simplification

$$||\mathbf{F}_a||_2 \begin{bmatrix} \cos\gamma_0 \\ \sin\gamma_0 \end{bmatrix} - ||\mathbf{F}_t||_2 \begin{bmatrix} \cos\psi \\ \sin\psi \end{bmatrix} + \begin{bmatrix} ||\mathbf{F}_{\text{drag}}||_2 \\ ||\mathbf{F}_g||_2 \end{bmatrix} = 0 \tag{45}$$

where ψ is the angle between the tether and the ground and $||\mathbf{F}_{\text{drag}}||_2$ is the negated x component of the aerodynamic force, $(\mathbf{F}_a)_A$. On average, ψ is equal to the rotation of the tracking curve, i.e., $\psi = \psi_0$.

As in [53], we multiply both sides by $[\sin\psi, -\cos\psi]^T$, which cancels out the effect of the tether, allowing us to solve for γ_0, which in turn leads to the theoretical efficiency factor

$$e = \cos^3\left(\psi_0 + \sin^{-1}\left(\frac{||\mathbf{F}_{\text{drag}}||_2}{||\mathbf{F}_a||_2}\sin\psi_0 + \frac{||\mathbf{F}_g||_2}{||\mathbf{F}_a||_2}\cos\psi_0\right)\right) \tag{46}$$

Finally, we calculate the theoretical maximum power that the hybrid control setup could obtain as

$$\tilde{P} = eA_{\text{eff}}\zeta\frac{1}{2}\rho||\mathbf{v}_{\text{W}}||_2^3 \tag{47}$$

When evaluated and averaged, this equates to a theoretical average power of 5.56 kW. Thus the hybrid control setup comes close to the upper bound that could be achieved.

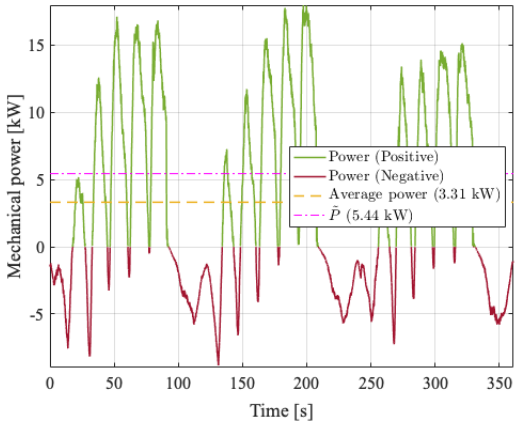

Fig. 15 The power P_{mech} that is generated at the ground station during flight.

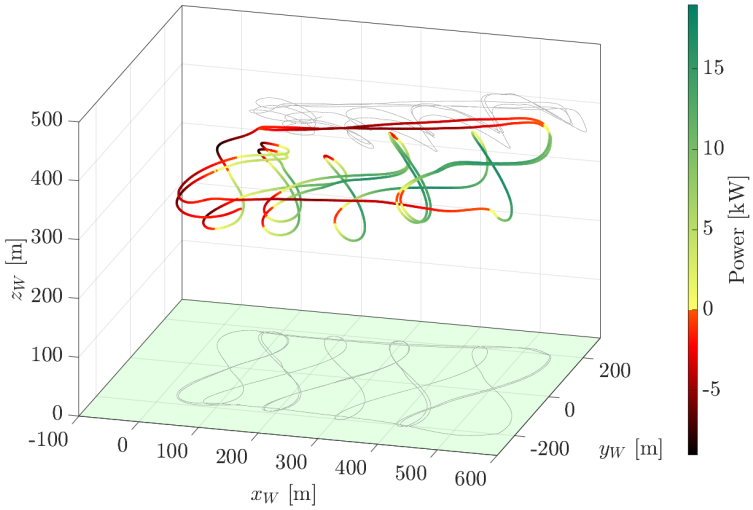

Fig. 16 Generated power in relation to the aircraft's flight path. Negative (resp. positive) power indicates a reeling in (resp. out) by the winch thus power is exerted (resp. harvested).

VI. Conclusion

We introduce a novel avoidance maneuver for the path-following controller of an AWE system through the introduction of a low-dimensional simplification of the system dynamics and application of HJ reachability analysis. Utilizing the presented switching law, the avoidance maneuver can be used in conjunction with an arbitrary primary flight controller for safe and power-optimal flight. We demonstrate the efficacy of the hybrid control setup through a full-scale simulation with a wind turbulence model, actuator delays, and nonlinear tether dynamics, validating that the chosen simplifications and worst-case considerations in the controller synthesis are sufficient for ensuring safe flight and avoiding a critical tether rupture.

Appendix

Coordinate transformation matrices

For brevity, we only list the transformation matrices in one direction, as the inverse transformation is obtained by simply transposing the appropriate matrix, since all transformation matrices are orthogonal [54, pg. 87].

$$\mathbf{M}_{\mathrm{AB}} = \begin{bmatrix} \cos\alpha_\mathrm{a}\cos\beta_\mathrm{a} & \sin\beta_\mathrm{a} & \sin\alpha_\mathrm{a}\cos\beta_\mathrm{a} \\ -\cos\alpha_\mathrm{a}\sin\beta_\mathrm{a} & \cos\beta_\mathrm{a} & -\sin\alpha_\mathrm{a}\sin\beta_\mathrm{a} \\ -\sin\alpha_\mathrm{a} & 0 & \cos\alpha_\mathrm{a} \end{bmatrix}, \quad \mathbf{M}_{\tau\mathrm{W}} = \begin{bmatrix} -\sin\phi\cos\lambda & -\sin\phi\sin\lambda & \cos\phi \\ -\sin\lambda & \cos\lambda & 0 \\ -\cos\phi\cos\lambda & -\cos\phi\sin\lambda & -\sin\phi \end{bmatrix} \tag{48}$$

$$\mathbf{M}_{\mathrm{OW}} = \begin{bmatrix} \cos\xi & \sin\xi & 0 \\ \sin\xi & -\cos\xi & 0 \\ 0 & 0 & -1 \end{bmatrix}, \quad \mathbf{M}_{\overline{\mathrm{A}}\mathrm{A}} = \begin{bmatrix} 1 & 0 & 0 \\ 0 & \cos\mu_\mathrm{a} & -\sin\mu_\mathrm{a} \\ 0 & \sin\mu_\mathrm{a} & \cos\mu_\mathrm{a} \end{bmatrix}, \quad \mathbf{M}_{\overline{\mathrm{A}}\mathrm{O}} = \begin{bmatrix} \cos\chi_\mathrm{a}\cos\gamma_\mathrm{a} & \sin\chi_\mathrm{a}\cos\gamma_\mathrm{a} & -\sin\gamma_\mathrm{a} \\ -\sin\chi_\mathrm{a} & \cos\chi_\mathrm{a} & 0 \\ \cos\chi_\mathrm{a}\sin\gamma_\mathrm{a} & \sin\chi_\mathrm{a}\sin\gamma_\mathrm{a} & \cos\gamma_\mathrm{a} \end{bmatrix} \tag{49}$$

Acknowledgments

The authors would like to acknowledge Dr. Sebastian Rapp, Dylan Eijkelhof, and Prof. Roland Schmehl for making their simulation framework available, as well as Jesse Hummel for helpful discussions on control strategies within the AWE community.

References

[1] IEA, "Wind Power," , November 2021. URL `https://www.iea.org/reports/wind-power`.

[2] Schmehl, R., *Airborne Wind Energy: Advances in Technology Development and Research*, Springer, Singapore, 2018. https://doi.org/10.1007/978-981-10-1947-0.

[3] Commission, E., for Research, D.-G., and Innovation, *Study on challenges in the commercialisation of airborne wind energy systems*, Publications Office, 2018. https://doi.org/10.2777/87591.

[4] Fagiano, L., Zgraggen, A. U., Morari, M., and Khammash, M., "Automatic crosswind flight of tethered wings for airborne wind energy: Modeling, control design, and experimental results," *IEEE Transactions on Control Systems Technology*, Vol. 22, No. 4, 2014, pp. 1433–1447. https://doi.org/10.1109/TCST.2013.2279592.

[5] Cherubini, A., Papini, A., Vertechy, R., and Fontana, M., "Airborne Wind Energy Systems: A review of the technologies," *Renewable and Sustainable Energy Reviews*, Vol. 51, 2015, pp. 1461–1476. https://doi.org/10.1016/j.rser.2015.07.053.

[6] Vermillion, C., Cobb, M., Fagiano, L., Leuthold, R., Diehl, M., Smith, R. S., Wood, T. A., Rapp, S., Schmehl, R., Olinger, D., and Demetriou, M., "Electricity in the air: Insights from two decades of advanced control research and experimental flight testing of airborne wind energy systems," *Annual Reviews in Control*, Vol. 52, 2021, pp. 330–357. https://doi.org/10.1016/j.arcontrol.2021.03.002.

[7] Fagiano, L., Quack, M., Bauer, F., Carnel, L., and Oland, E., "Autonomous Airborne Wind Energy Systems: Accomplishments and Challenges," *Annual Review of Control, Robotics, and Autonomous Systems*, Vol. 5, No. 1, 2022, pp. 603–631. https://doi.org/10.1146/annurev-control-042820-124658.

[8] Eijkelhof, D., Rapp, S., Fasel, U., Gaunaa, M., and Schmehl, R., "Reference Design and Simulation Framework of a Multi-Megawatt Airborne Wind Energy System," *Journal of Physics: Conference Series*, Vol. 1618, No. 3, 2020. https://doi.org/10.1088/1742-6596/1618/3/032020.

[9] Salma, V., Friedl, F., and Schmehl, R., "Improving reliability and safety of airborne wind energy systems," *Wind Energy*, Vol. 23, No. 2, 2020, pp. 340–356. https://doi.org/10.1002/we.2433.

[10] Williams, P., Lansdorp, B., and Ockesl, W., "Optimal Crosswind Towing and Power Generation with Tethered Kites," *Journal of Guidance, Control, and Dynamics*, Vol. 31, No. 1, 2008, pp. 81–93. https://doi.org/10.2514/1.30089.

[11] Fagiano, L., Milanese, M., and Piga, D., "Optimization of airborne wind energy generators," *International Journal of Robust and Nonlinear Control*, Vol. 22, No. 18, 2012, pp. 2055–2083. https://doi.org/10.1002/rnc.1808.

[12] Lucia, S., and Engell, S., "Control of towing kites under uncertainty using robust economic nonlinear model predictive control," *2014 European Control Conference (ECC)*, 2014, pp. 1158–1163. https://doi.org/10.1109/ECC.2014.6862335.

[13] Erhard, M., and Strauch, H., "Flight control of tethered kites in autonomous pumping cycles for airborne wind energy," *Control Engineering Practice*, Vol. 40, 2015, pp. 13–26. https://doi.org/10.1016/j.conengprac.2015.03.001.

[14] Licitra, G., Koenemann, J., Bürger, A., Williams, P., Ruiterkamp, R., and Diehl, M., "Performance assessment of a rigid wing Airborne Wind Energy pumping system," *Energy*, Vol. 173, 2019, pp. 569–585. https://doi.org/10.1016/j.energy.2019.02.064.

[15] Fisac, J. F., Akametalu, A. K., Zeilinger, M. N., Kaynama, S., Gillula, J., and Tomlin, C. J., "A General Safety Framework for Learning-Based Control in Uncertain Robotic Systems," *IEEE Transactions on Automatic Control*, Vol. 64, No. 7, 2019, pp. 2737–2752. https://doi.org/10.1109/TAC.2018.2876389.

[16] Rapp, S., and Schmehl, R., "Enhancing Resilience of Airborne Wind Energy Systems Through Upset Condition Avoidance," *Journal of Guidance, Control, and Dynamics*, Vol. 44, No. 2, 2021, pp. 251–265. https://doi.org/10.2514/1.G005189.

[17] Rapp, S., "Robust Automatic Pumping Cycle Operation of Airborne Wind Energy Systems Rapp,," Ph.D. thesis, Delft University of Technology, 2021. https://doi.org/10.4233/uuid:ab2adf33-ef5d-413c-b403-2cfb4f9b6bae.

[18] Lu, P., van Kampen, E.-J., de Visser, C., and Chu, Q., "Aircraft fault-tolerant trajectory control using Incremental Nonlinear Dynamic Inversion," *Control Engineering Practice*, Vol. 57, 2016, pp. 126–141. https://doi.org/10.1016/j.conengprac.2016.09.010.

[19] Bansal, S., Chen, M., Herbert, S., and Tomlin, C. J., "Hamilton-Jacobi reachability: A brief overview and recent advances," *2017 IEEE 56th Annual Conference on Decision and Control (CDC)*, 2017, pp. 2242–2253. https://doi.org/10.1109/CDC.2017.8263977.

[20] Vertovec, N., Ober-Blöbaum, S., and Margellos, K., "Multi-objective low-thrust spacecraft trajectory design using reachability analysis," *European Journal of Control*, Vol. 69, 2023, p. 100758. https://doi.org/10.1016/j.ejcon.2022.100758.

[21] Chen, M., Herbert, S. L., Vashishtha, M. S., Bansal, S., and Tomlin, C. J., "Decomposition of Reachable Sets and Tubes for a Class of Nonlinear Systems," *IEEE Transactions on Automatic Control*, Vol. 63, No. 11, 2018. https://doi.org/10.1109/TAC.2018.2797194.

[22] Malz, E., Koenemann, J., Sieberling, S., and Gros, S., "A reference model for airborne wind energy systems for optimization and control," *Renewable Energy*, Vol. 140, 2019, pp. 1004–1011. https://doi.org/10.1016/j.renene.2019.03.111.

[23] Rapp, S., and Schmehl, R., "Vertical takeoff and landing of flexible wing kite power systems," *Journal of Guidance, Control, and Dynamics*, Vol. 41, No. 11, 2018, pp. 2386–2400. https://doi.org/10.2514/1.G003535.

[24] Fechner, U., van der Vlugt, R., Schreuder, E., and Schmehl, R., "Dynamic model of a pumping kite power system," *Renewable Energy*, Vol. 83, 2015, pp. 705–716. https://doi.org/10.1016/j.renene.2015.04.028.

[25] Jehle, C., and Schmehl, R., "Applied tracking control for kite power systems," *Journal of Guidance, Control, and Dynamics*, Vol. 37, No. 4, 2014, pp. 1211–1222. https://doi.org/10.2514/1.62380.

[26] Loyd, M. L., "Crosswind Kite Power." *Journal of energy*, Vol. 4, No. 3, 1980, pp. 106–111. https://doi.org/10.2514/3.48021.

[27] Luchsinger, R. H., "Pumping cycle kite power," *Green Energy and Technology*, 2013, pp. 47–64. https://doi.org/10.1007/978-3-642-39965-7_3.

[28] Zgraggen, A. U., Fagiano, L., and Morari, M., "Automatic Retraction and Full-Cycle Operation for a Class of Airborne Wind Energy Generators," *IEEE Transactions on Control Systems Technology*, Vol. 24, No. 2, 2016, pp. 594–608. https://doi.org/10.1109/TCST.2015.2452230.

[29] Todeschini, D., Fagiano, L., Micheli, C., and Cattano, A., "Control of a rigid wing pumping Airborne Wind Energy system in all operational phases," *Control Engineering Practice*, Vol. 111, 2021, p. 104794. https://doi.org/10.1016/j.conengprac.2021.104794.

[30] Berra, A., and Fagiano, L., "An optimal reeling control strategy for pumping airborne wind energy systems without wind speed feedback," *2021 European Control Conference (ECC)*, 2021, pp. 1199–1204. https://doi.org/10.23919/ECC54610.2021.9655018.

[31] Rapp, S., Schmehl, R., Oland, E., and Haas, T., "Cascaded pumping cycle control for rigid wing airborne wind energy systems," *Journal of Guidance, Control, and Dynamics*, Vol. 42, No. 11, 2019, pp. 2456–2473. https://doi.org/10.2514/1.G004246.

[32] "MATLAB Aerospace Toolbox," , 2021a. The MathWorks, Natick, MA, USA.

[33] "U.S. Military Handbook MIL-HDBK-1797B," , April 2012.

[34] Diehl, M., "Airborne wind energy: Basic concepts and physical foundations," *Airborne Wind Energy*, edited by U. Ahrens, M. Diehl, and R. Schmehl, Green Energy and Technology, Springer Berlin Heidelberg, Berlin, Heidelberg, 2013, pp. 3–22. https://doi.org/10.1007/978-3-642-39965-7.

[35] Erhard, M., and Strauch, H., "Theory and experimental validation of a simple comprehensible model of tethered kite dynamics used for controller design," *Green Energy and Technology*, 2013, pp. 141–166. https://doi.org/10.1007/978-3-642-39965-7_8/COVER.

[36] Erhard, M., and Strauch, H., "Control of towing kites for seagoing vessels," *IEEE Transactions on Control Systems Technology*, Vol. 21, 2013, pp. 1629–1640. https://doi.org/10.1109/TCST.2012.2221093.

[37] Canale, M., Fagiano, L., and Milanese, M., "High Altitude Wind Energy Generation Using Controlled Power Kites," *IEEE Transactions on Control Systems Technology*, Vol. 18, No. 2, 2010, pp. 279–293. https://doi.org/10.1109/TCST.2009.2017933.

[38] Erhard, M., Horn, G., and Diehl, M., "A quaternion-based model for optimal control of an airborne wind energy system," *ZAMM - Journal of Applied Mathematics and Mechanics / Zeitschrift für Angewandte Mathematik und Mechanik*, Vol. 97, No. 1, 2017, pp. 7–24. https://doi.org/10.1002/zamm.201500180.

[39] Campi, M. C., and Garatti, S., *Introduction to the Scenario Approach*, Society for Industrial and Applied Mathematics, Philadelphia, PA, 2018. https://doi.org/10.1137/1.9781611975444.

[40] Fagiano, L., and Novara, C., "Automatic crosswind flight of tethered wings for airborne wind energy: a direct data-driven approach," *IFAC Proceedings Volumes*, Vol. 47, No. 3, 2014, pp. 4927–4932. https://doi.org/10.3182/20140824-6-ZA-1003.01896, 19th IFAC World Congress.

[41] Schmidt, E., De Lellis Costa de Oliveira, M., Saraiva da Silva, R., Fagiano, L., and Trofino Neto, A., "In-Flight Estimation of the Aerodynamics of Tethered Wings for Airborne Wind Energy," *IEEE Transactions on Control Systems Technology*, Vol. 28, No. 4, 2020, pp. 1309–1322. https://doi.org/10.1109/TCST.2019.2907663.

[42] Oprea, J., *Differential geometry and its applications*, 2nd ed., Mathematical Association of America, Washington, D.C., 2007. https://doi.org/https://doi.org/10.1090/clrm/059.

[43] Liberzon, D., *Switching in Systems and Control*, Birkhäuser Boston, 2003. https://doi.org/10.1007/978-1-4612-0017-8.

[44] Vertovec, N., Ober-Blöbaum, S., and Margellos, K., "Verification of safety critical control policies using kernel methods," *2022 European Control Conference (ECC)*, 2022, pp. 1870–1875. https://doi.org/10.23919/ECC55457.2022.9838224.

[45] Margellos, K., and Lygeros, J., "Hamilton-jacobi formulation for reach-avoid differential games," *IEEE Transactions on Automatic Control*, Vol. 56, No. 8, 2011, pp. 1849–1861. https://doi.org/10.1109/TAC.2011.2105730.

[46] Varaiya, P. P., "On the Existence of Solutions to a Differential Game," *SIAM Journal on Control*, Vol. 5, No. 1, 1967, pp. 153–162. https://doi.org/10.1137/0305009.

[47] Evans, L., and Souganidis, P. E., "Differential games and representation formulas for solutions of Hamilton-Jacobi-Isaacs equations," *Indiana Univ. Math. J*, Vol. 33, No. 5, 1984, pp. 773–797. https://doi.org/10.1512/iumj.1984.33.33040.

[48] Osher, S., and Fedkiw, R., *Level Set Methods and Dynamic Implicit Surfaces*, Applied Mathematical Sciences, Springer New York, 2003. https://doi.org/10.1007/b98879.

[49] Bansal, S., and Tomlin, C. J., "DeepReach: A Deep Learning Approach to High-Dimensional Reachability," *2021 IEEE International Conference on Robotics and Automation (ICRA)*, 2021, pp. 1817–1824. https://doi.org/10.1109/ICRA48506.2021.9561949.

[50] Mitchell, I. M., "The flexible, extensible and efficient toolbox of level set methods," *Journal of Scientific Computing*, Vol. 35, No. 2-3, 2008, pp. 300–329. https://doi.org/10.1007/s10915-007-9174-4.

[51] Gillula, J. H., and Tomlin, C. J., "Guaranteed Safe Online Learning via Reachability: tracking a ground target using a quadrotor," *2012 IEEE International Conference on Robotics and Automation*, 2012, pp. 2723–2730. https://doi.org/10.1109/ICRA.2012.6225136.

[52] Hespanha, J. P., "Hybrid Control and Switched Systems, Lecture Notes," , 2005. URL https://web.ece.ucsb.edu/~hespanha/ece229/.

[53] Costello, S., Costello, C., François, G., and Bonvin, D., "Analysis of the maximum efficiency of kite-power systems," *Journal of Renewable and Sustainable Energy*, Vol. 7, No. 5, 2015, pp. 1–16. https://doi.org/10.1063/1.4931111.

[54] Nair, M. T., and Singh, A., *Linear algebra*, Springer, Singapore, 2018. https://doi.org/10.1007/978-981-13-0926-7.